Title

An interpretable flux-based machine learning model of drug interactions across metabolic space and time

Authors

Carolina H. Chung,[1] Sriram Chandrasekaran[1–4]*

Affiliations

[1]Department of Biomedical Engineering, University of Michigan, Ann Arbor, MI, 48109, USA.
[2]Program in Chemical Biology, University of Michigan, Ann Arbor, MI, 48109, USA.
[3]Center for Bioinformatics and Computational Medicine, Ann Arbor, MI, 48109, USA.
[4]Rogel Cancer Center, University of Michigan Medical School, Ann Arbor, MI, 48109, USA.
*Corresponding author: csriram@umich.edu

Abstract

Drug combinations are a promising strategy to counter antibiotic resistance. However, current experimental and computational approaches do not account for the entire complexity involved in combination therapy design, such as the effect of the growth environment, drug order, and time interval. To address these limitations, we present an approach that uses genome-scale metabolic modeling and machine learning to explain and guide combination therapy design. Our approach (a) accommodates diverse data types, (b) accurately predicts drug interactions in various growth conditions, (c) accounts for time- and order-specific interactions, and (d) identifies mechanistic factors driving drug interactions. The entropy in bacterial stress response, time between treatments, and gluconeogenesis activation were the most predictive features of combination therapy outcomes across time scales and growth conditions. Analysis of the vast landscape of condition-specific drug interactions revealed promising new drug combinations and a tradeoff in the efficacy between simultaneous and sequential combination therapies.

Introduction

Antimicrobial resistance (AMR) occurs due to extended exposure to antibiotics, which allow bacteria to evolve and genetically adapt to promote their survival. These genetic changes culminate in the development of resistance mechanisms that render antibiotic treatments ineffective (*1*). In the context of AMR, bacterial metabolism plays a key role in promoting survival in new niches through adaptable use of nutrients in the local environment (*2*, *3*). Bacterial metabolism also impacts susceptibility to treatment, such as through the production of reactive oxygen species (*4*, *5*) or changes in membrane permeability (*6*). Of note, these metabolic responses are tied to entropy (i.e., disorder) in the bacterial stress response, which has been shown to be a generalizable predictor for antibiotic sensitivity (*7*). Altogether, these individual findings suggest that changes in bacterial metabolism in response to antibiotics may be insightful for the design of novel treatments that mitigate resistance.

Combination therapy, which involves the use of two or more therapeutics, holds great potential for combating resistant pathogens as it not only leverages already regulated therapeutics (*8*), but also offers room for improved efficacy (*9*). Further, combination therapy could be optimized to selectively target resistant pathogens via collateral sensitivity, which has been shown to overcome multidrug resistance in cancer (*10*, *11*). Collateral sensitivity entails the increased sensitivity to a therapeutic that results from initial treatment with another stress agent (*12*). This phenomenon has been observed across various diseases and organisms (*10*, *13–15*), and in context of AMR, could be leveraged to prevent and mitigate resistance (*16*). Combination therapies are traditionally identified using experimental methods; however, this approach quickly becomes infeasible when considering high-order combinations, the effects of the growth media, and time-/order-dependence for treatment efficacy.

With the advent of high-throughput omics data and application of machine learning (ML), it is now possible to expedite the search for effective combination therapies. ML has also been applied to reveal mechanistic insights into antibiotic mechanisms of action (*17*, *18*) and identify novel antibacterial compounds (*19*, *20*). In the past decade, several groups have used these methods to computationally design combination therapies in context of cancer (*21–26*) and AMR (*27–29*). For the latter case, prior models have been shown to generate predictions that accurately correspond to experimental and clinical efficacy against *Escherichia coli* and *Mycobacterium tuberculosis*, thus offering effective reduction of the search space for combination therapies against AMR (*27*, *29*). However, these approaches are limited by the availability of omics data measuring the bacterial response to antibiotic treatment. The combined drug effect on bacterial growth has also only been assessed in a limited number of growth environments (*28*). Moreover, current models have primarily focused on simultaneous combinations; consequently, the potential of designing time- and order-dependent combination therapies that promote collateral sensitivity remains unexplored.

To address these limitations, we present an approach that integrates genome-scale metabolic models (GEMs) into ML model development to determine effective combination therapies. Using GEMs allows us to integrate diverse data types and account for different pathogen growth conditions. GEMs are computational models built from gene-protein-reaction associations of metabolic genes present in the genome of an organism (*30*). Additionally, they include annotation of traditional antibiotic targets such as cell wall synthesis, DNA

replication, and RNA transcription. Model constraints, such as from omics data or nutrient availability, can be imposed to simulate bacterial metabolism in response to different perturbations (*31*, *32*). Our approach using GEMs and ML provides a systems-level perspective of the bacterial response to antibiotic treatment in condition-specific cases. This is critical for designing efficacious combination therapies, since experimentally measured susceptibility to antibiotics *in vitro* may not always translate into efficacy *in vivo*. We further extend our approach to predict outcomes for sequential combination therapies, which can be designed into cyclic antibiotic regimens that mitigate resistance (*16*). Finally, we showcase how our models reveal mechanistic insights that explain treatment potency and can be leveraged to finetune data-driven combination therapy design.

Results

CARAMeL is a hybrid GEM–ML approach that predicts combination therapy outcomes

Our approach, called *Condition-specific Antibiotic Regimen Assessment using Mechanistic Learning* (*CARAMeL*), involves a two-step modeling process: (a) simulating metabolic flux data using GEMs and (b) developing a ML model to predict combination therapy outcomes using flux from GEMs. For the first part, omics data and metabolite composition of the extracellular environment serve as GEM inputs to determine flux profiles in response to drug treatment and growth in defined media, respectively (***Fig. 1A***). For the second part, GEM-derived flux profiles and drug interaction data serve as inputs to train a ML model that predicts interaction outcomes for novel drug combinations (***Fig. 1B***). We developed ML models predictive of combination therapy outcomes for *E. coli* and *M. tb* using the Random Forests algorithm. We specifically chose this ML method as it can handle small datasets and determine feature importance, i.e., how much each feature contributes to the accuracy in model predictions. The feature importance can reveal mechanistic insights into the factors driving combination therapy outcomes.

We determined metabolic flux profiles in response to drug treatment and condition-specific growth by constraining the *E. coli* GEM iJO1366 (*33*) and the *M. tb* GEM iEK1011 (*34*). For drug flux profiles, we imposed chemogenomic data for *E. coli* (*35*) and transcriptomic data for *M. tb* (*29*) as GEM constraints. Briefly, chemogenomic data measures single-gene knockout (KO) fitness while transcriptomics data measures genome-wide expression of genes. By selecting genes for which there was differential fitness or expression in response to a specific treatment, we could infer a set of differentially regulated genes for individual drugs. For transcriptomic data, positive and negative differential expression directly corresponded with up- and down-regulation, respectively. For chemogenomic data, we surmised based on the cost-benefit gene expression model (*36*) that gene KOs resulting in low fitness were up-regulated while gene KOs that enhanced fitness (i.e., large benefit) were down-regulated. Direct comparison of flux profiles simulated from a chemogenomic-based approach against flux profiles simulated with transcriptomics and proteomics data confirmed that these assumptions were valid (***Fig. S1***) (*37–39*). To determine growth media flux profiles, the availability of metabolites within a media condition was used to constrain the GEMs. Specifically, we modified the uptake rate for exchange reactions providing key metabolites (e.g., glycerol exchange for M9 glycerol media) to allow cellular intake (see ***Methods*** for further details).

Prior to ML model development, we processed drug and media flux profiles to determine joint profiles for all combinations of interest. Joint profiles were comprised of four pieces of information: (a) the combined effect of all treatments (i.e., sigma scores), (b) the unique

effect of individual treatments (i.e., delta scores), (c) the overall metabolic entropy (i.e., entropy scores), and (d) time interval (relevant for time- and order-dependent combinations). To determine sigma and delta scores, we adapted a strategy previously used for creating joint chemogenomic profiles (*27*, *28*). Specifically, we binarized drug and media flux profiles based on differential flux activity in comparison to baseline (i.e., GEM simulation without additional constraints). Sigma scores were defined as the union of binarized flux profiles for all treatments involved in a combination. Delta scores for simultaneous interactions were defined as the symmetric difference between flux profiles, while delta scores for sequential interactions were determined based on the treatment sequence for a combination (see ***Methods*** for details). To account for metabolic entropy, we first calculated entropy as defined by Zhu *et al.* (*7*) for each drug and media flux profile. We then defined entropy scores as the mean and sum of entropy among all treatments involved in a combination. Finally, the time feature was defined as the time interval between the first and last treatments for a combination (see ***Methods*** and ***Fig. S2*** for further details).

Using feature (i.e., joint profiles) and outcome (i.e., interaction scores, IS) information for a set of drug combinations, we trained ML models to associate feature patterns to drug combination outcomes. Next, we used the trained ML models to predict outcomes for new drug combinations based on their feature information alone. We then compared our predictions against experimental data by calculating the Spearman correlation. We also assessed model performance by calculating the area under the receiver operating curve (AUROC) for both synergy and antagonism. High and positive values for both metrics indicate that model predictions correspond well with actual drug interaction outcomes.

CARAMeL predicts drug combination efficacy against E. coli and M. tb with high accuracy

We benchmarked CARAMeL against previous approaches by directly comparing our prediction accuracy against those reported in literature and those re-calculated using omics data directly instead of using fluxes. For these comparisons, we trained ML models and evaluated their performance for five different cases:

1. Predicting novel pairwise drug interaction outcomes for *E. coli* (*27*)
2. Predicting novel three-way drug interaction outcomes for *E. coli* (*28*)
3. Predicting pairwise drug interaction outcomes for *E. coli* cultured in a novel nutrient condition (M9 glycerol media) (*28*)
4. Predicting novel pairwise and three-way interaction outcomes for *M. tb* (*29*)
5. Predicting interaction outcomes for pairwise to five-way TB regimens used in clinical trials (*40*)

Of note, the first, second, and fourth cases tested the model's ability to predict unseen combinations involving test drugs with new mechanisms of action. The third case assessed whether the model could predict drug interaction outcomes in a new growth environment, while the fifth case ascertained if predicted outcomes corresponded with clinical efficacy. ***Fig. 2*** summarizes our findings for all analyses listed above. For all these studies, the same train-test datasets were used for evaluating CARAMeL against the original methods to ensure direct comparison. The same thresholds for synergy and antagonism defined in the original studies were also used in all these comparisons. Further discussion on ML model development and results, including the specific train-test allocation of interaction data reported in literature for each case, is provided below.

For case 1, we used drug interaction data previously measured for 171 pairwise combinations involving 19 drugs that cover a diverse set of targets (*27*) (***Table S1***). Out of this total, 105 interactions involving 15 drugs were used for model training and the remaining 66 interactions, which involved four new drugs that introduced new mechanisms of action (e.g., RNA synthesis), were used for model validation. The CARAMeL model yielded significant correlations between experimental and predicted scores ($R = 0.65$, $p \sim 10^{-9}$, ***Fig. S3A***). Model predictions also yielded high AUROC values for classifying synergy ($IS < -0.5$, AUROC = 0.75) and antagonism ($IS > 2$, AUROC = 0.82) (***Fig. S3B***) based on thresholds defined in the original study. Of note, these results were considerably better than those reported in literature ($R = 0.52$) (*27*) and were comparable to the omic-based approach ($R = 0.63$) (***Fig. 2A***).

For case 2, we re-trained the CARAMeL model using 171 pairwise interactions to predict 56 three-way combinations involving eight antibiotics (*28*) (***Table S1***). Our model generated accurate predictions ($R = 0.63$, $p \sim 10^{-7}$, ***Fig. S3C***) and notably identified synergistic interactions ($IS < -0.2$, AUROC = 0.95, ***Fig. S3D***) with higher accuracy than the omics-based approach (AUROC = 0.76, ***Fig. 2B***).

For case 3, the CARAMeL model was once again re-trained with the 171 pairwise interactions and additional pairwise data measured for *E. coli* cultured in M9 glucose and lysogeny broth (LB) media. We then applied our model to predict 55 pairwise interaction outcomes for *E. coli* cultured in M9 glycerol media. Our model yielded results comparable to those from literature (*28*) and re-determined using omics data across all three performance measures (***Figs. 2, S3E, and S3F***).

For case 4, we trained a CARAMeL model using combination data for *M. tb* treated with 196 pairwise to five-way interactions involving 40 drugs (*29*) (***Table S2***). We then used data for 36 unseen interactions for model validation. The CARAMeL model yielded predictions that significantly correlated with experimental data ($R = 0.57$, $p \sim 10^{-4}$, ***Fig. S4A***) and performed well in classifying synergistic ($IS < 0.9$, AUROC = 0.82) and antagonistic ($IS > 1.1$, AUROC = 0.84) interactions (***Fig. S4B***). Though the CARAMeL-based correlation is slightly lower than that reported in literature (*29*) ($R = 0.63$), our model classified both synergistic and antagonistic interactions with high accuracies that are comparable to a model trained on omics data (***Fig. 2B***).

For case 5, we used the same CARAMeL model from case 4 to predict interaction outcomes for 57 multi-drug TB regimens involving nine drugs prescribed in separate clinical trials (*40*) (***Table S2***). Of note, interaction outcomes for this dataset measured regimen efficacy based on sputum clearance after two months of treatment. We found that model predictions were significantly correlated ($R = 0.52$, $p \sim 10^{-5}$, ***Fig. S4C***) with sputum clearance, and that model predictions classified as synergistic ($IS < 0.9$) captured most of the efficacious treatments (sputum clearance > 80%) amongst all 57 TB regimens (***Fig. S4D***). These results were comparable to both literature- (*29*) and omic-based results across all three performance measurements (***Fig. 2***). Overall, we found that our approach retained high accuracies in predicting combination therapy outcomes for a diverse set of test cases based on *E. coli* and *M. tb* data. This is striking considering that CARAMeL solely relies on simulated metabolic information, which was determined using only ~25–35% of available omics data.

CARAMeL enables large-scale investigation of combination therapy outcome in different growth environments

To demonstrate the power of using GEMs in predicting condition-specific combination therapy outcomes, we applied the CARAMeL approach to predict pairwise drug interactions in multiple media conditions. For this task, we used experimental data for *E. coli* treated with four single drug treatments (AZTreonam, CEFoxitin, TETtracycline, TOBramycin) and two pairwise drug treatments (CEF + TET, CEF + TOB) (***Table S3***). Of note, this treatment panel evaluated the metabolic response in *E. coli* to bactericidal (i.e., death-inducing) and bacteriostatic (i.e., growth-inhibiting) drugs, both individually and in combination. Each drug treatment outcome was assessed in *E. coli* cultured in Biolog phenotype microarray (PM) (*41*) plate-1, which measured metabolic respiration in 96 carbon sources (***Fig. 3A***). Out of these 96 media conditions, 57 could be simulated based on the metabolites annotated in the *E. coli* GEM. As a result, ML model development and all downstream analyses were conducted using the data subset pertaining to the 57 media conditions that were simulated.

We constructed a ML model using the following inputs: flux profiles for the four drug treatments as well as the 57 media conditions, and interaction outcomes for 228 (4 * 57) drug-media combinations. We then evaluated our model by predicting outcomes for 114 (2 * 57) drug-drug-media combinations (***Fig. 3B***). Overall, we found that model predictions significantly correlated with experimental outcomes ($R = 0.62$, $p < 10^{-16}$, ***Fig. 3C***). We also assessed correlations specific to each drug pair and found that model predictions still corresponded well with experimental data (CEF+TET: $R = 0.58$, $p \sim 10^{-6}$, CEF+TOB: $R = 0.78$, $p < 10^{-16}$). This large-scale inspection of combination therapy outcome in different growth environments was only possible with the CARAMeL approach, where flux profiles could be determined for 57 media conditions. A direct comparison of the same scale was not possible with the omic-based approach, as chemogenomic data was only available for five media conditions. Moreover, our approach enables combination therapy design for condition-specific cases. This is critical for successful clinical translation, considering that the predominant carbon source can change depending on where bacteria reside inside the host (*2*).

The CARAMeL approach was extended to predict outcomes for sequential interactions

Current approaches for predicting combination therapy outcomes focus on drug treatments that are given simultaneously. Here, we extended our approach to predict treatment efficacy for time- and order-dependent (i.e., sequential) interactions. In contrast to simultaneous combinations, the order and length of each drug treatment dictates how a pathogen adapts itself, and in turn, influences its sensitivity to successive drug treatments. As such, interaction outcomes are interpreted as leading to collateral sensitivity (analogous to synergy) or cross-resistance (analogous to antagonism). For this task, we used data for *E. coli* evolved in single drug treatments for three timespans (10, 21, and 90 days) then subsequently treated with a second drug (*38*, *42*, *43*). To account for both time- and order-dependent drug effect, we re-defined the delta scores for sequential joint profiles. Briefly, delta scores were defined as the difference in binarized drug profiles normalized by the total treatment time (mathematically defined for pairwise sequences below):

$$\delta = \frac{t_2 v_2 - t_1 v_1}{\left(t_1 + t_2\right)} \qquad \textit{Eq. 1}$$

where δ = delta scores, t = length of treatment time, and v = binarized flux profile.

To initially assess how well the CARAMeL approach could predict sequential treatment outcomes, we first conducted a 10-fold cross-validation of the sequential data (N = 628), which involved 27 unique drugs (***Table S4***). We found that CARAMeL predictions moderately, but significantly, correlated with experimental outcomes ($R = 0.50$, $p < 10^{-16}$, ***Fig. 4A***). Further, the model performed well in determining whether a sequential interaction resulted in collateral sensitivity (IS < -0.1, AUROC = 0.76) or cross-resistance (IS > 0.1, AUROC = 0.76) (***Fig. 4D***).

We next evaluated the extent of our model's predictive power by conducting two types of leave-out analyses: (a) leave-first-drug-out and (b) leave-second-drug-out. The first case tested whether the model could generalize sequential treatment outcomes for an unknown evolved strain, while the second case assessed whether the model could generalize the immediate effect of a drug on strains evolved in other drugs. For a leave-out analysis, all interactions involving the drug of interest in the appropriate sequence position (first or second) were left out of model training and instead predicted for by the trained model. Similar to the cross-validation analysis, model performance was measured by the overall Spearman correlation and AUROC values for collateral sensitivity and cross-resistance. We found that both leave-out analyses yielded predictions similar to those attained from cross-validation (***Figs. 4B, 4C, 4E, and 4F***). Overall, these results indicate that CARAMeL generates robust and accurate predictions for sequential interactions.

Treatment time and entropy are key factors that determine combination therapy potency

To gain mechanistic insight into which factors influence combination therapy outcomes, we trained a CARAMeL model using all interaction data available for *E. coli*. Broadly, this included three sets of simultaneous combinations (*27*, *28*) (including data from our Biolog experiment) and three sets of sequential interactions (*38*, *42*, *43*). To account for differing units of measurement between datasets, we scaled interaction scores according to the following formula:

$$x_{scaled} = \frac{x}{max|x|} \qquad Eq.\ 2$$

where x is a vector of interaction scores for a given dataset. Of note, we applied a $\log_2$ transformation to the Biolog data prior to scaling this dataset using *Eq. 2*. These steps constrained all interaction scores to range between ±1 while retaining the sign consensus for classifying interactions based on their score (negative IS → synergy, positive IS → antagonism). In total, we trained our model on 1,308 drug interactions and attained highly accurate predictions ($R = 0.80$, $p < 10^{-16}$) for both synergistic (IS < -0.1, AUROC = 0.80) and antagonistic (IS > 0.1, AUROC = 0.91) interactions.

Using the Random Forests algorithm, we ranked features by their predictive importance based on how the model accuracy decreases when a feature is removed (***Methods***). As our model was trained on both simultaneous and sequential interactions, four types of features were provided: (a) sigma scores (combined effect), (b) delta scores (unique effect), (c) metabolic entropy, and (d) time interval between treatments. Interestingly, the time feature was found to be most important (***Data S1***). This highlights the fact that the outcome for a drug combination can greatly differ when treatments are given simultaneously versus when they are prescribed in a sequential manner. This can be seen when we compare interaction

scores for simultaneous and sequential treatments involving the same set of drugs (***Fig. 5A***). For example, collateral sensitivity frequently arises when *E. coli* is first weakened by an aminoglycoside and then treated with an antibiotic from another class, potentially due to a reduction in the proton-motive force across the inner membrane (*44*). However, synergy is not frequently observed for this set of drug combinations when given simultaneously. Another example is the case when *E. coli* is first treated with a quinolone then exposed to an antibiotic from another class. This type of sequence generally leads to cross-resistance (*45*), likely due to increased DNA damage by quinolones (*46*), but no trend towards synergy or antagonism is observed when the drugs are given simultaneously (***Fig. 5A***).

In addition to time, entropy was a top predictor that distinguished between different interaction types. Specifically, antagonistic and cross-resistant interactions seemed to impose lower overall entropy in the metabolic response to drug treatment compared to neutral interactions ($p < 0.05$) and those leading to synergy or collateral sensitivity (***Fig. 5B***). Previously, Zhu *et al*. found that low fitness and bacterial sensitivity to antibiotics are associated with large transcriptional disorder (*7*). Interestingly, here we found that cross-resistant and antagonistic interactions generally imposed less metabolic disarray than synergistic or additive (i.e., neutral) interactions. These observations indicate that the bacterial stress response, as measured via entropy, is a useful proxy to determine how antagonistic a combination therapy will be regardless of treatment time or order.

Top CARAMeL features mechanistically explain combination efficacy in different carbon sources

Including time and entropy, we found that 652 features explained 95% of the variance in model predictions (***Data S1***). We subsequently determined that the differential flux through 244 out of the 360 GEM reactions associated with these top features significantly distinguished between synergistic and antagonistic interactions (two-sample t-test, p-value < 0.05, ***Data S2***). Finally, we deduced that 13 metabolic pathways were enriched by this set of 244 reactions (***Table 1***). Differential activity through these pathways aligned with the expected metabolic response to antibiotic treatments. For example, increased flux through DNA repair systems (e.g., nucleotide salvage) is an expected response after exposure to quinolones, which target DNA gyrase (*47*). Differential flux through transport reactions is also an expected response that decreases drug concentrations within the bacterial cell, therefore minimizing their adverse effects on fitness (*48*).

Beyond explaining general metabolic responses to antibiotic stress, our top model predictors also revealed insights into the efficacy for drug treatments used in our Biolog experiment. Among the 244 reactions deduced from top model predictors, we found that increased flux through fructose 1,6-bisphosphatase (FBPase) led to significantly greater efficacy for all six drug treatment conditions (two-sample t-test, $p < 0.05$, ***Fig. 6A***). FBPase is an enzyme active during gluconeogenesis and catalyzes the conversion of fructose 1,6-bisphosphate to fructose 6-phosphate. Upon assessing which PM01 conditions induced increased flux through FBPase, we found that the vast majority contained carbon sources downstream of the last step in glycolysis, which produces pyruvate (***Data S3***). Increased FBPase activity within these conditions is most likely explained by the need to activate gluconeogenesis to synthesize the cell wall and other biomass precursors for optimal growth (*49*). Of note, antagonism is predicted to occur due to opposing drug effects on cellular respiration (*50*). By increasing flux towards the TCA cycle, gluconeogenic substrates may reduce the potential for antagonistic metabolic effects (*51*) and, in turn, increase drug potency (***Fig.***

6B). Activation of gluconeogenesis is also essential for *E. coli* and *M. tb* growth *in vivo* (*52*, *53*). This observation could be used to design synergistic therapies that are effective *in vivo*.

Screening candidate therapies with robust synergy and collateral sensitivity

Synergy observed in the lab may not result in synergy *in vivo* due to differences in growth conditions or drug pharmacokinetics, wherein drugs may reach the infection site at different times rather than simultaneously (*54*). Considering these factors, combination therapies that show synergy across growth conditions and time scales hold the best potential for successful clinical translation. To discover such therapies, we predicted pairwise regimen outcomes for all drugs for which the *E. coli* CARAMeL model was trained on (N = 33). For each drug pair, we evaluated three cases: (a) simultaneous treatment (D_1 + D_2), (b) sequential treatment from D_1 to D_2, and (c) sequential treatment from D_2 to D_1. For sequential interactions, we set the duration for the first treatment to 14 days, based on the most commonly prescribed antibiotic treatment duration against bloodstream infection by Enterobacteriaceae (*55*), and one day for the second treatment. In total, we generated predictions for 90,288 combinations that differed based on interaction type and growth environment ($_{33}C_2$ pairs x 3 types x 57 PM01 growth conditions, ***Data S4***).

Out of the 528 ($_{33}C_2$) drug pairs that we screened, 190 were predicted to yield synergy for at least one case out of 171 (3 types x 57 PM01 conditions) (***Fig. 7A***). Surprisingly, only a small subset (N = 6) were predicted to be both synergistic ($IS_{simultaneous} < 0$) and lead to collateral sensitivity ($IS_{sequential} < 0$) consistently across multiple (N > 10) carbon sources (***Data S5, Figs. 7B and 7C***). Interestingly, only one drug pair (amikacin-ampicillin) was robustly synergistic across all three cases (D_1 + D_2, $D_1 \rightarrow D_2$, $D_2 \rightarrow D_1$). Amikacin-ampicillin treatment has previously been shown to be clinically effective for a wide range of infections (*56–58*) including treatment of bacteremia in neutropenic patients (*59*) and neonatal bacterial infections (*60*). Increased sensitivity to ampicillin or amikacin in both simultaneous and sequential scenarios has also been experimentally observed (*61*). Collateral sensitivity in ampicillin → amikacin treatment is most likely explained by increased amikacin penetration that occurs after cell wall disruption by ampicillin (a beta-lactam) (*62*). For the reverse case (amikacin → ampicillin treatment), the predicted synergy is most likely explained by the increased sensitivity due to disrupted membrane potential and ROS generation that typically occur when *E. coli* is first treated with an aminoglycoside (*44*, *63–65*).

The remaining four drug pairs involved interactions between rifampicin, tetracycline, azithromycin, and fusidic acid. One pair (rifampicin-azithromycin) has demonstrated clinical efficacy in treating arthritis (*66*) induced by pathogenic Chlamydia (Gram-negative). Another pair (rifampicin-fusidic acid) has shown clinical efficacy against prosthetic joint infection caused by drug-resistant staphylococci (Gram-positive) (*67*). Drug treatment with rifampicin combined with minocycline (a tetracycline derivative) has also been shown to prevent colonization by slime-producing staphylococci in catheters (*68*). Of note, rifampicin-minocycline, as well as rifampicin combined with other drugs, has been advised as treatment for Gram-negative and non-mycobacterial infections (*69*, *70*). Further investigation into these combinations may be of interest considering the ever-present concern over bacterial resistance to rifampicin (*71*).

Discussion

Here we introduced CARAMeL, a modeling approach to design condition-specific antibiotic regimens. We have shown that CARAMeL can be extended to account for the growth environment and sequential drug interactions. Ultimately, CARAMeL offers multiple advantages over prior methods of similar nature. First, our approach enables use of diverse data sources (e.g., chemogenomics, transcriptomics) and/or their combined use, therefore maximizing the number of drugs that are screened. Moreover, the use of GEMs enables simulation of highly tunable growth conditions, which may be leveraged to investigate combination therapy outcomes in the host environment. We also extended our approach to factor different time intervals when designing combination therapies, which may be critical for mitigating resistance.

Most importantly, the CARAMeL model provides systems-level insight into factors that influence treatment potency. First, combination therapy outcome is highly dependent on how drugs are prescribed together (simultaneously vs. sequentially). Hence, solely optimizing synergy of simultaneous treatments may unintentionally exacerbate AMR. Analysis of the drug interaction landscape suggests that only a small fraction (< 1%) of screened combinations show robust synergy across growth conditions and time intervals: amikacin-ampicillin, rifampicin-azithromycin, rifampicin-fusidic acid, rifampicin-tetracycline, tetracycline-fusidic acid, and vancomycin-fusidic acid. Clinical evidence for efficacy exists for the first four regimens (*57–60*, *66–70*), while the last two may be worth investigating as potential additions to our therapeutic arsenal against AMR.

Secondly, we affirmed that system-wide entropy is a generalizable predictor for antibiotic sensitivity and can be used to identify antagonistic interactions between combinations of stressors. Thirdly, we showed that all six drug treatments used in our Biolog experiment were significantly more potent in gluconeogenic carbon sources. This heightened potency may be explained by increased flux through the TCA cycle that reduces antagonistic effects (***Fig. 6B***).

Although the use of GEMs in CARAMeL offers major advantages with data compatibility, condition tunability, and mechanistic insight, it also introduces some limitations. The level of accuracy and thoroughness in GEM annotation may influence CARAMeL model performance. Moreover, our current approach only provides a "snapshot" perspective of the metabolic response to a condition. This may be a potential reason for the slightly diminished CARAMeL model performance in predicting sequential outcomes. Nevertheless, these are areas that can be addressed with continued curation of GEMs (*72*) and advances in dynamic metabolic modeling (*73*). Overall, the ability to simulate specific growth environments offers the potential to evaluate treatment efficacy *in vivo* and advance clinical translation of novel antibiotic regimens. Moreover, these combination therapies could restore use of defunct antibiotics against resistant pathogens while mitigating further resistance (*16*, *74*).

Materials and Methods

Experimental Design (Biolog Phenotype Microarray)

E. coli MG1655 was cultured in Biolog phenotype microarray (PM) 1, which screened bacterial growth in 95 carbon sources and a negative control (i.e., water) (*41*). *E. coli* was subsequently treated with six distinct drug treatments in duplicate: aztreonam (0.03 ug/mL), cefoxitin (1.87 ug/mL), tetracycline (1.42 ug/mL), tobramycin (0.15 ug/mL), cefoxitin (1.87 ug/mL) + tetracycline (1.42 ug/mL), and cefoxitin (1.87 ug/mL) + tobramycin (1.42 ug/mL). Including a reference plate (*E. coli* growth in PM01 only), phenotype in each treatment was colorimetrically measured in duplicate using tetrazolium violet dye, which quantifies cellular respiration. All experimental procedures, data collection, and quality control were performed at Biolog, Inc. The area under the respiration curve was calculated using MATLAB and reported as the ratio of treatment to reference.

Simulating Metabolic Flux using GEMs

The *E. coli* GEM iJO1366 (*33*) and the *M. tb* GEM iEK1008 (*34*) were used to simulate metabolic fluxes at steady-state. To simulate drug flux profiles, chemogenomic data for *E. coli* (*35*) and transcriptomic data for *M. tb* (*29*) served as GEM constraints. Specifically, differential gene regulation in response to drug treatment was uniquely inferred from each dataset. For chemogenomic data, which measured single-gene knockout (KO) fitness, genes whose KOs promoted growth were assumed as dispensable while gene KOs that resulted in low fitness were assumed to be essential for growth in said condition. Based on these assumptions, genes corresponding with low ($z < -2$) and high ($z > 2$) fitness were inferred to be up- and down-regulated, respectively. For transcriptomic data, which measured single-gene expression, up- and down-regulation were directly inferred based on high ($z > 2$) and low ($z < -2$) expression values, respectively. These processes yielded individual sets of differentially regulated genes that were integrated into corresponding GEMs using a linear optimization version of the integrative metabolic analysis tool (iMAT) algorithm (*75*, *76*). To determine media flux profiles, metabolite availability was computationally defined by constraining exchange reactions annotated in iJO1366. For each carbon source of interest (e.g., glycerol), the lower bound (i.e., uptake rate) for the corresponding exchange reaction (e.g., glycerol exchange) was set to -10 to allow cellular intake.

Of note, use of the linear iMAT algorithm required constraint-based modeling (CBM) parameter fine-tuning for three variables: kappa, rho, and epsilon (*77*). Kappa and rho serve as relative weights for "off" and "on" reactions associated with the differentially expressed genes, respectively, in their contribution to the objective function. Epsilon represents the minimum flux through "on" reactions. For the purposes of this research, we varied all three parameter values from 10^{-3} to 1 and determined the optimal parameter set based on three criteria: (1) maximizing the Spearman correlation between predicted and actual interaction scores after 10-fold cross-validation using a training dataset, (2) minimizing the number of conditions simulated to have no growth, and (3) ensuring non-zero variability in the simulated growth rates between conditions. ***Table S5*** provides results for all three assessments for all parameter sets of interest. The following optimal parameter values were obtained for each GEM using the training dataset: (1) iJO1366 – kappa $=10^{-2}$, rho $= 10^{-2}$, epsilon = 1, and (2) iEK1008 – kappa $= 10^{-2}$, rho $= 10^{-2}$, epsilon $= 10^{-2}$. These parameter values were used for all results when benchmarking CARAMeL against previous approaches based on *E. coli* and *M. tb* drug interaction datasets (***Table S6***).

Data Processing to Determine Joint Profiles

Flux profiles were used to define joint profiles for each drug combination, which were comprised of four pieces of information: sigma scores, delta scores, cumulative entropy, and length of treatment interval (***Fig. S2***). Sigma and delta scores were representative of the combined and unique effect of drugs involved in a combination, respectively. Both score types were determined after flux profiles were binarized based on differential flux activity (either positive or negative) in comparison to baseline, mathematically defined below:

$$v_{i,\,positive} = \begin{cases} 1 & \dfrac{v_{i,\,treatment}}{v_{i,\,baseline}} > 2 \\ 0 & otherwise \end{cases}, \; v \in \mathbb{R}^m \qquad Eq.\ 3a$$

$$v_{i,\,negative} = \begin{cases} 1 & \dfrac{v_{i,\,treatment}}{v_{i,\,baseline}} < -2 \\ 0 & otherwise \end{cases}, \; v \in \mathbb{R}^m \qquad Eq.\ 3b$$

where v = reaction flux and m = total number of GEM reactions. Sigma scores were mathematically defined for both simultaneous and sequential interactions using the following equation:

$$\sigma_i = \frac{2}{n}\sum_{j=1}^{n} v_{i,\,j}, \; v \in \mathbb{R}^{m \times n} \qquad Eq.\ 4$$

where σ = sigma score, v = binarized flux profile, m = total number of GEM reactions, and n = total number of conditions in a combination. Delta scores were separately defined for simultaneous and sequential interactions based on *Eq. 5a* and *Eq. 5b*, respectively:

$$\delta_i = \begin{cases} 1 & \sum_{j=1}^{n} v_{i,\,j} = 1 \\ 0 & otherwise \end{cases}, \; v \in \mathbb{R}^{m \times n} \qquad Eq.\ 5a$$

$$\delta_i = t_n v_{i,\,n} - \sum_{j=1}^{n-1} t_j v_{i,\,j}, \; t \in \mathbb{R}^n, \; v \in \mathbb{R}^{m \times n} \qquad Eq.\ 5b$$

where δ = delta score, t = treatment time, v = binarized flux profile, m = total number of GEM reactions, and n = total number of conditions in a combination. Cumulative entropy features were determined by processing non-binarized flux profiles in two steps. First, metabolic entropy for each condition was mathematically defined by the following equation:

$$H_j = \ln\left(\sigma_j^2\right) \qquad Eq.\ 6$$

where H_j = entropy and σ_j^2 = variance in non-binarized flux profile. Of note, this formulation was adapted from Zhu *et al.*, who quantified entropy of the bacterial stress response to antibiotics (*7*). Next, the mean and sum in entropy for all conditions involved in an interaction were used to define two distinct entropy features. Finally, the time feature was defined as the time interval between the first and last treatment for a combination. For simultaneous interactions, the time feature was set to zero.

ML Model Development using Random Forests

All CARAMeL models were built in MATLAB (Mathworks, Inc.) using the regression-based Random Forests (RF) algorithm (*78*). Briefly, RF is an ensemble method comprised of decision trees that learn to associate feature information to a target variable. For the

regression-based approach, the RF model returns the mean prediction from all decision trees. To develop CARAMeL models, joint profiles served as feature information while drug interaction scores were used as the target variable. Interaction scores were quantified using the Loewe additivity model (*79*), which is based on drug concentrations (refer to the original sources of drug interaction datasets for further details in score calculation). Both joint profiles and interactions scores for drug combinations of interest were used as model inputs during training, while only joint profiles were provided as input during model testing. Default values for all other model parameters were used during both training and testing.

ML Model Performance Assessment

Model performance was evaluated based on two metrics: (1) the Spearman correlation between actual and predicted interaction scores and (2) the area under the receiver operating curve (AUROC) for classifying interactions as synergistic or antagonistic. Of note, model predictions for TB regimens used in clinical trials were negative transformed before being compared to clinical outcomes. Since these clinical trials reported percentage of patients that were cured, we would expect to see a negative correlation between interaction scores and clinical efficacy, with synergistic regimens (IS < -0.1) performing better than antagonistic regimens. The sign for the scores were hence flipped to maintain a positive correlation indicating good model performance. Classification of simultaneous drug interactions was based on score threshold values reported in the original literature for a dataset. For both sequential interactions and the CARAMeL model trained on all interaction data for *E. coli*, interaction scores were first scaled by the maximum absolute value (*Eq. 2*). Interaction values below -0.1 and above 0.1 were then used to classify interactions as synergistic and antagonistic, respectively. For the 10-fold cross-validation analysis conducted for sequential interactions, the interaction data was randomly partitioned into ten subsets of similar size (N ~ 63). CARAMeL was then applied to predict each subset at a time, where the given subset was left out of the model training (i.e., the remaining 90% of the data was used to train the model). All model predictions were then compared to the sequential data as a whole to calculate the overall Spearman correlation and AUROC values.

CARAMeL Top Feature Extraction

Top features were determined based on their ranked importance in generating accurate predictions. To calculate feature importance, each feature was first left out of model training and testing. The mean squared error (MSE) between predicted and true interaction scores was then calculated for each model. Finally, feature importance was measured as the increase in MSE for a model lacking a feature compared to the model trained on all features. After ranking features according to decreasing importance, the first set of features amounting to a cumulative importance of 0.95 (corresponding to 95% variance explained) were selected for downstream model interpretation and analysis.

Statistical Analysis

A one-way analysis of variance (ANOVA) test was used to compare both the entropy mean and entropy sum of drug interactions grouped by their classification (synergy, neutral, antagonism). A multiple comparison test based on Tukey's honestly significant difference (HSD) was subsequently performed to identify statistically significant pairwise differences using a p-value threshold of 0.05. A two-sample Student's t-test with unequal variance was used to define which reactions distinguished between synergistic and antagonistic interactions based on differential flux activity. The same test was used to determine significant differences in drug treatment potency between carbon sources with and without

differential flux through FBPase. Lastly, a hypergeometric test was conducted to determine significantly enriched metabolic pathways based on GEM reactions associated with top CARAMeL predictors. For this test, the total number of reactions annotated in iJO1366 corresponded with the population size.

References

1. J. M. A. Blair, M. A. Webber, A. J. Baylay, D. O. Ogbolu, L. J. V Piddock, Molecular mechanisms of antibiotic resistance. *Nat. Rev. Microbiol.* **13** (2015), pp. 42–51.
2. S. A. Brown, K. L. Palmer, M. Whiteley, Revisiting the host as a growth medium. *Nat. Rev. Microbiol.* **6** (2008), pp. 657–666.
3. T. M. Fuchs, W. Eisenreich, J. Heesemann, W. Goebel, Metabolic adaptation of human pathogenic and related nonpathogenic bacteria to extra- and intracellular habitats. *FEMS Microbiol. Rev.* **36** (2012), pp. 435–462.
4. M. A. Kohanski, D. J. Dwyer, B. Hayete, C. A. Lawrence, J. J. Collins, A Common Mechanism of Cellular Death Induced by Bactericidal Antibiotics. *Cell*. **130**, 797–810 (2007).
5. A. T. Dharmaraja, Role of Reactive Oxygen Species (ROS) in Therapeutics and Drug Resistance in Cancer and Bacteria. *J. Med. Chem.* **60**, 3221–3240 (2017).
6. J. L. Martínez, F. Rojo, Metabolic regulation of antibiotic resistance. *FEMS Microbiol. Rev.* **35**, 768–789 (2011).
7. Z. Zhu, D. Surujon, J. C. Ortiz-Marquez, W. Huo, R. R. Isberg, J. Bento, T. van Opijnen, Entropy of a bacterial stress response is a generalizable predictor for fitness and antibiotic sensitivity. *Nat. Commun.* **11**, 1–15 (2020).
8. M. A. Farha, E. D. Brown, Drug repurposing for antimicrobial discovery. *Nat. Microbiol.* **4** (2019), pp. 565–577.
9. M. Tyers, G. D. Wright, Drug combinations: a strategy to extend the life of antibiotics in the 21st century. *Nat. Rev. Microbiol.* **17** (2019), pp. 141–155.
10. K. M. Pluchino, M. D. Hall, A. S. Goldsborough, R. Callaghan, M. M. Gottesman, Collateral sensitivity as a strategy against cancer multidrug resistance. *Drug Resist. Updat.* **15**, 98–105 (2012).
11. S. Vijayaraghavalu, J. K. Dermawan, V. Cheriyath, V. Labhasetwar, Highly synergistic effect of sequential treatment with epigenetic and anticancer drugs to overcome drug resistance in breast cancer cells is mediated via activation of p21 gene expression leading to G2/M cycle arrest. *Mol. Pharm.* **10**, 337–352 (2013).
12. C. Pál, B. Papp, V. Lázár, Collateral sensitivity of antibiotic-resistant microbes. *Trends Microbiol.* **23** (2015), pp. 401–407.
13. G. Gadamski, D. Ciarka, J. Gressel, S. W. Gawronski, Negative cross-resistance in triazine-resistant biotypes of Echinochloa crus-galli and Conyza canadensis. *Weed Sci.* **48**, 176–180 (2000).
14. S. G. Deeks, Treatment of antiretroviral-drug-resistant HIV-1 infection. *Lancet*. **362** (2003), pp. 2002–2011.
15. A. K. Lukens, L. S. Ross, R. Heidebrecht, F. J. Gamo, M. J. Lafuente-Monasterio, M. L. Booker, D. L. Hartl, R. C. Wiegand, D. F. Wirth, Harnessing evolutionary fitness in Plasmodium falciparum for drug discovery and suppressing resistance. *Proc. Natl. Acad. Sci. U. S. A.* **111**, 799–804 (2014).
16. M. Baym, L. K. Stone, R. Kishony, Multidrug evolutionary strategies to reverse antibiotic resistance. *Science (80-.).* **351**, aad3292–aad3292 (2016).
17. J. H. Yang, S. N. Wright, M. Hamblin, B. O. Palsson, G. C. Walker, J. J. Collins, A White-Box Machine Learning Approach for Revealing Antibiotic Mechanisms of Action. *Cell*.

177, 1649–1661 (2019).

18. B. Ribeiro da Cunha, L. P. Fonseca, C. R. C. Calado, Simultaneous elucidation of antibiotic mechanism of action and potency with high-throughput Fourier-transform infrared (FTIR) spectroscopy and machine learning. *Appl. Microbiol. Biotechnol.* **105**, 1269–1286 (2021).
19. J. M. Stokes, K. Yang, K. Swanson, W. Jin, A. Cubillos-Ruiz, N. M. Donghia, C. R. MacNair, S. French, L. A. Carfrae, Z. Bloom-Ackerman, V. M. Tran, A. Chiappino-Pepe, A. H. Badran, I. W. Andrews, E. J. Chory, G. M. Church, E. D. Brown, T. S. Jaakkola, R. Barzilay, J. J. Collins, A Deep Learning Approach to Antibiotic Discovery. *Cell*. **180**, 688–702 (2020).
20. S. S. El Zahed, E. D. Brown, Chemical-Chemical Combinations Map Uncharted Interactions in Escherichia coli under Nutrient Stress, doi:10.1016/j.isci.2018.03.018.
21. X.-M. Zhao, M. Iskar, G. Zeller, M. Kuhn, V. van Noort, P. Bork, Prediction of Drug Combinations by Integrating Molecular and Pharmacological Data. *PLoS Comput. Biol.* **7**, e1002323 (2011).
22. J.-H. Lee, D. G. Kim, T. J. Bae, K. Rho, J.-T. Kim, J.-J. Lee, Y. Jang, B. C. Kim, K. M. Park, S. Kim, CDA: Combinatorial Drug Discovery Using Transcriptional Response Modules. *PLoS One*. **7**, e42573 (2012).
23. H. E. Chua, S. S. Bhowmick, L. Tucker-Kellogg, Synergistic target combination prediction from curated signaling networks: Machine learning meets systems biology and pharmacology. *Methods*. **129**, 60–80 (2017).
24. K. E. Regan-Fendt, J. Xu, M. DiVincenzo, M. C. Duggan, R. Shakya, R. Na, W. E. Carson, P. R. O. Payne, F. Li, Synergy from gene expression and network mining (SynGeNet) method predicts synergistic drug combinations for diverse melanoma genomic subtypes. *npj Syst. Biol. Appl.* **5**, 1–15 (2019).
25. B. Yuan, C. Shen, A. Luna, A. Korkut, D. S. Marks, J. Ingraham, C. Sander, CellBox: Interpretable Machine Learning for Perturbation Biology with Application to the Design of Cancer Combination Therapy. *Cell Syst.* **12**, 128-140.e4 (2021).
26. T. Zhang, L. Zhang, P. R. O. Payne, F. Li, in *Methods in Molecular Biology* (Humana Press Inc., 2021; https://pubmed.ncbi.nlm.nih.gov/32926369/), vol. 2194, pp. 223–238.
27. S. Chandrasekaran, M. Cokol-Cakmak, N. Sahin, K. Yilancioglu, H. Kazan, J. J. Collins, M. Cokol, Chemogenomics and orthology-based design of antibiotic combination therapies. *Mol. Syst. Biol.* **12**, 872 (2016).
28. M. Cokol, C. Li, S. Chandrasekaran, Chemogenomic model identifies synergistic drug combinations robust to the pathogen microenvironment. *PLOS Comput. Biol.* **14**, e1006677 (2018).
29. S. Ma, S. Jaipalli, J. Larkins-Ford, J. Lohmiller, B. B. Aldridge, D. R. Sherman, S. Chandrasekaran, Transcriptomic signatures predict regulators of drug synergy and clinical regimen efficacy against tuberculosis. *MBio*. **10** (2019), doi:10.1128/mBio.02627-19.
30. N. D. Price, J. L. Reed, B. Palsson, Genome-scale models of microbial cells: Evaluating the consequences of constraints. *Nat. Rev. Microbiol.* **2** (2004), pp. 886–897.
31. N. E. Lewis, H. Nagarajan, B. O. Palsson, Constraining the metabolic genotype-phenotype relationship using a phylogeny of in silico methods. *Nat. Rev. Microbiol.* **10** (2012), pp. 291–305.
32. S. Dahal, J. T. Yurkovich, H. Xu, B. O. Palsson, L. Yang, Synthesizing Systems Biology Knowledge from Omics Using Genome-Scale Models. *Proteomics*. **20** (2020), p. 1900282.
33. J. D. Orth, T. M. Conrad, J. Na, J. A. Lerman, H. Nam, A. M. Feist, B. Ø. Palsson, A comprehensive genome-scale reconstruction of *Escherichia coli* metabolism—2011. *Mol. Syst. Biol.* **7**, 535 (2011).

34. E. S. Kavvas, Y. Seif, J. T. Yurkovich, C. Norsigian, S. Poudel, W. W. Greenwald, S. Ghatak, B. O. Palsson, J. M. Monk, Updated and standardized genome-scale reconstruction of Mycobacterium tuberculosis H37Rv, iEK1011, simulates flux states indicative of physiological conditions. *BMC Syst. Biol.* **12**, 25 (2018).
35. R. J. Nichols, S. Sen, Y. J. Choo, P. Beltrao, M. Zietek, R. Chaba, S. Lee, K. M. Kazmierczak, K. J. Lee, A. Wong, M. Shales, S. Lovett, M. E. Winkler, N. J. Krogan, A. Typas, C. A. Gross, Phenotypic landscape of a bacterial cell. *Cell*. **144**, 143–56 (2011).
36. E. Dekel, U. Alon, Optimality and evolutionary tuning of the expression level of a protein. *Nature*. **436**, 588–592 (2005).
37. T. Maeda, J. Iwasawa, H. Kotani, N. Sakata, M. Kawada, T. Horinouchi, A. Sakai, K. Tanabe, C. Furusawa, High-throughput laboratory evolution reveals evolutionary constraints in Escherichia coli. *Nat. Commun.* **11**, 5970 (2020).
38. S. Suzuki, T. Horinouchi, C. Furusawa, Prediction of antibiotic resistance by gene expression profiles. *Nat. Commun.* **5**, 5792 (2014).
39. M. Mori, Z. Zhang, A. Banaei-Esfahani, J. Lalanne, H. Okano, B. C. Collins, A. Schmidt, O. T. Schubert, D. Lee, G. Li, R. Aebersold, T. Hwa, C. Ludwig, From coarse to fine: the absolute Escherichia coli proteome under diverse growth conditions. *Mol. Syst. Biol.* **17**, e9536 (2021).
40. L. J. Bonnett, G. Ken-Dror, G. C. K. W. Koh, G. R. Davies, Comparing the Efficacy of Drug Regimens for Pulmonary Tuberculosis: Meta-analysis of Endpoints in Early-Phase Clinical Trials. *Clin. Infect. Dis.* **46**, 46–54 (2017).
41. B. R. Bochner, P. Gadzinski, E. Panomitros, Phenotype Microarrays for high-throughput phenotypic testing and assay of gene function. *Genome Res.* **11**, 1246–1255 (2001).
42. L. Imamovic, M. O. A. Sommer, Use of collateral sensitivity networks to design drug cycling protocols that avoid resistance development. *Sci. Transl. Med.* **5**, 204ra132-204ra132 (2013).
43. T. Oz, A. Guvenek, S. Yildiz, E. Karaboga, Y. T. Tamer, N. Mumcuyan, V. B. Ozan, G. H. Senturk, M. Cokol, P. Yeh, E. Toprak, Strength of selection pressure is an important parameter contributing to the complexity of antibiotic resistance evolution. *Mol. Biol. Evol.* **31**, 2387–2401 (2014).
44. V. Lázár, G. Pal Singh, R. Spohn, I. Nagy, B. Horváth, M. Hrtyan, R. Busa-Fekete, B. Bogos, O. Méhi, B. Csörgő, G. Pósfai, G. Fekete, B. Szappanos, B. Kégl, B. Papp, C. Pál, Bacterial evolution of antibiotic hypersensitivity. *Mol. Syst. Biol.* **9**, 700 (2013).
45. C. C. Sanders, W. E. Sanders, R. V. Goering, V. Werner, Selection of multiple antibiotic resistance by quinolones, β-lactams, and aminoglycosides with special reference to cross-resistance between unrelated drug classes. *Antimicrob. Agents Chemother.* **26**, 797–801 (1984).
46. C. C. Sanders, Mechanisms responsible for cross-resistance and dichotomous resistance among the quinolones. *Clin. Infect. Dis.* **32** (2001), pp. 1–8.
47. A. Fàbrega, S. Madurga, E. Giralt, J. Vila, Mechanism of action of and resistance to quinolones. *Microb. Biotechnol.* **2**, 40–61 (2009).
48. S. B. Levy, Active efflux, a common mechanism for biocide and antibiotic resistance. *J. Appl. Microbiol.* **92**, 65S-71S (2002).
49. A. Varma, B. O. Palsson, Metabolic capabilities of escherichia coli. II. Optimal growth patterns. *J. Theor. Biol.* **165**, 503–522 (1993).
50. M. A. Lobritz, P. Belenky, C. B. M. Porter, A. Gutierrez, J. H. Yang, E. G. Schwarz, D. J. Dwyer, A. S. Khalil, J. J. Collins, Antibiotic efficacy is linked to bacterial cellular respiration. *Proc. Natl. Acad. Sci. U. S. A.* **112**, 8173–8180 (2015).
51. M. K. Oh, J. C. Liao, Gene expression profiling by DNA microarrays and metabolic fluxes

in Escherichia coli. *Biotechnol. Prog.* **16**, 278–286 (2000).
52. Y. Bertin, C. Deval, A. De La Foye, L. Masson, V. Gannon, J. Harel, C. Martin, M. Desvaux, E. Forano, The gluconeogenesis pathway is involved in maintenance of enterohaemorrhagic Escherichia coli O157:H7 in bovine intestinal content. *PLoS One*. **9**, e98367 (2014).
53. J. Marrero, K. Y. Rhee, D. Schnappinger, K. Pethe, S. Ehrt, Gluconeogenic carbon flow of tricarboxylic acid cycle intermediates is critical for Mycobacterium tuberculosis to establish and maintain infection. *Proc. Natl. Acad. Sci. U. S. A.* **107**, 9819–9824 (2010).
54. J. M. Cicchese, A. Sambarey, D. Kirschner, J. J. Linderman, S. Chandrasekaran, A multi-scale pipeline linking drug transcriptomics with pharmacokinetics predicts in vivo interactions of tuberculosis drugs. *Sci. Rep.* **11**, 5643 (2021).
55. G. S. Tansarli, N. Andreatos, E. E. Pliakos, E. Mylonakis, A Systematic Review and Meta-analysis of Antibiotic Treatment Duration for Bacteremia Due to Enterobacteriaceae. *Antimicrob. Agents Chemother.* **63** (2019), doi:10.1128/AAC.02495-18.
56. K. M. Krause, A. W. Serio, T. R. Kane, L. E. Connolly, Aminoglycosides: An overview. *Cold Spring Harb. Perspect. Med.* **6** (2016), doi:10.1101/cshperspect.a027029.
57. Guidelines for the management of adults with hospital-acquired, ventilator-associated, and healthcare-associated pneumonia. *Am. J. Respir. Crit. Care Med.* **171** (2005), pp. 388–416.
58. R. P. Dellinger, M. Levy, A. Rhodes, D. Annane, H. Gerlach, S. M. Opal, J. E. Sevransky, C. L. Sprung, I. S. Douglas, R. Jaeschke, T. M. Osborn, M. E. Nunnally, S. R. Townsend, K. Reinhart, R. M. Kleinpell, D. C. Angus, C. S. Deutschman, F. R. Machado, G. D. Rubenfeld, S. A. Webb, R. J. Beale, J. L. Vincent, R. Moreno, L. Aitken, H. Al Rahma, G. R. Bernard, J. F. Bion, P. Biban, T. Calandra, J. A. Carcillo, T. P. Clemmer, J. V. Divatia, S. Fujishima, B. Du, S. Gando, G. Guyatt, C. Goodyear-Bruch, J. A. Hazelzet, S. M. Hollenberg, H. Hirasawa, J. Jacobi, R. M. Kacmarek, I. Jenkins, E. Jimenez, A. E. Jones, W. Kern, S. O. Koh, J. Kotani, F. Machado, J. Marini, J. C. Marshall, H. Masur, S. Mehta, J. Muscedere, L. M. Napolitano, M. M. Parker, J. E. Parrrillo, H. Qiu, A. G. Randolph, J. Rello, E. Resende, E. P. Rivers, C. A. Schorr, K. Shukri, E. Silva, M. D. Soth, A. E. Thompson, J. S. Vender, T. Welte, J. L. Zimmerman, Surviving sepsis campaign: International guidelines for management of severe sepsis and septic shock: 2012. *Crit. Care Med.* **41**, 580–637 (2013).
59. J. Palmblad, B. Lönnqvist, Combination of Amikacin and either Ampicillin or Cephalotin as Initial Treatment of Febrile Neutropenic Patients. *Acta Med. Scand.* **212**, 379–384 (1982).
60. M. A. Umaña, C. M. Odio, E. Castro, J. L. Salas, G. H. McCracken, Evaluation of aztreonam and ampicillin vs. amikacin and ampicillin for treatment of neonatal bacterial infections. *Pediatr. Infect. Dis. J.* **9**, 175–180 (1990).
61. V. Lorian, J. Ernst, Activity of amikacin and ampicillin in succession and in combination. *Diagn. Microbiol. Infect. Dis.* **11**, 163–169 (1988).
62. R. C. Moellering, C. Wennersten, A. N. Weinberg, Studies on antibiotic synergism against enterococci. I. Bacteriologic studies. *J. Lab. Clin. Med.* **77**, 821–828 (1971).
63. M. A. Kohanski, D. J. Dwyer, J. Wierzbowski, G. Cottarel, J. J. Collins, Mistranslation of Membrane Proteins and Two-Component System Activation Trigger Antibiotic-Mediated Cell Death. *Cell*. **135**, 679–690 (2008).
64. M. A. Kohanski, D. J. Dwyer, J. J. Collins, How antibiotics kill bacteria: From targets to networks. *Nat. Rev. Microbiol.* **8** (2010), pp. 423–435.
65. G. N. Bruni, J. M. Kralj, Membrane voltage dysregulation driven by metabolic dysfunction underlies bactericidal activity of aminoglycosides. *Elife*. **9**, 1–25 (2020).
66. J. D. Carter, L. R. Espinoza, R. D. Inman, K. B. Sneed, L. R. Ricca, F. B. Vasey, J.

Valeriano, J. A. Stanich, C. Oszust, H. C. Gerard, A. P. Hudson, Combination antibiotics as a treatment for chronic Chlamydia-induced reactive arthritis: A double-blind, placebo-controlled, prospective trial. *Arthritis Rheum.* **62**, 1298–1307 (2010).

67. W. Zimmerli, A. Trampuz, P. E. Ochsner, Current concepts: Prosthetic-joint infections. *N. Engl. J. Med.* **351**, 1645–1654 (2004).
68. I. Raad, R. Darouiche, R. Hachem, M. Sacilowski, G. P. Bodey, Antibiotics and prevention of microbial colonization of catheters. *Antimicrob. Agents Chemother.* **39**, 2397 (1995).
69. C. M. J. Drapeau, E. Grilli, N. Petrosillo, Rifampicin combined regimens for Gram-negative infections: data from the literature. *Int. J. Antimicrob. Agents*. **35**, 39–44 (2010).
70. G. N. Forrest, K. Tamura, Rifampin combination therapy for nonmycobacterial infections. *Clin. Microbiol. Rev.* **23** (2010), pp. 14–34.
71. A. Tupin, M. Gualtieri, F. Roquet-Banères, Z. Morichaud, K. Brodolin, J. P. Leonetti, Resistance to rifampicin: At the crossroads between ecological, genomic and medical concerns. *Int. J. Antimicrob. Agents*. **35** (2010), pp. 519–523.
72. D. B. Bernstein, S. Sulheim, E. Almaas, D. Segrè, Addressing uncertainty in genome-scale metabolic model reconstruction and analysis. *Genome Biol.* **22** (2021), pp. 1–22.
73. P. A. Saa, L. K. Nielsen, Formulation, construction and analysis of kinetic models of metabolism: A review of modelling frameworks. *Biotechnol. Adv.* **35** (2017), pp. 981–1003.
74. S. Kim, T. D. Lieberman, R. Kishony, Alternating antibiotic treatments constrain evolutionary paths to multidrug resistance. *Proc. Natl. Acad. Sci. U. S. A.* **111**, 14494–14499 (2014).
75. T. Shlomi, M. N. Cabili, M. J. Herrgård, B. Palsson, E. Ruppin, Network-based prediction of human tissue-specific metabolism. *Nat. Biotechnol.* **26** (2008), pp. 1003–1010.
76. F. Shen, L. Boccuto, R. Pauly, S. Srikanth, S. Chandrasekaran, Genome-scale network model of metabolism and histone acetylation reveals metabolic dependencies of histone deacetylase inhibitors. *Genome Biol.* **20**, 49 (2019).
77. F. Shen, C. Cheek, S. Chandrasekaran, Dynamic Network Modeling of Stem Cell Metabolism. *Methods Mol. Biol.* **1975**, 305–320 (2019).
78. L. Breiman, Random forests. *Mach. Learn.* **45**, 5–32 (2001).
79. S. Loewe, H. Muischnek, Über Kombinationswirkungen - Mitteilung: Hilfsmittel der Fragestellung. *Arch. für Exp. Pathol. und Pharmakologie*. **114**, 313–326 (1926).

Acknowledgments

We thank Brendan Lewis at Biolog for carrying out the Phenotype Microarray assays.

Funding:

National Institutes of Health grant R35 GM13779501 (SC)
National Institutes of Health NIAID R56AI150826 (SC)
University of Michigan faculty start-up fund (SC)

Author contributions:

Conceptualization: SC
Methodology: CHC, SC
Investigation: CHC, SC
Visualization: CHC
Supervision: SC
Writing—original draft: CHC
Writing—review & editing: CHC, SC

Competing interests:

The authors declare that they have no competing interests.

Data and materials availability:

All datasets and code used within this work are provided through the CARAMeL GitHub repository (https://github.com/sriram-lab/CARAMeL). Additional information on datasets and results are available in the supplementary materials.

FIGURES AND TABLES

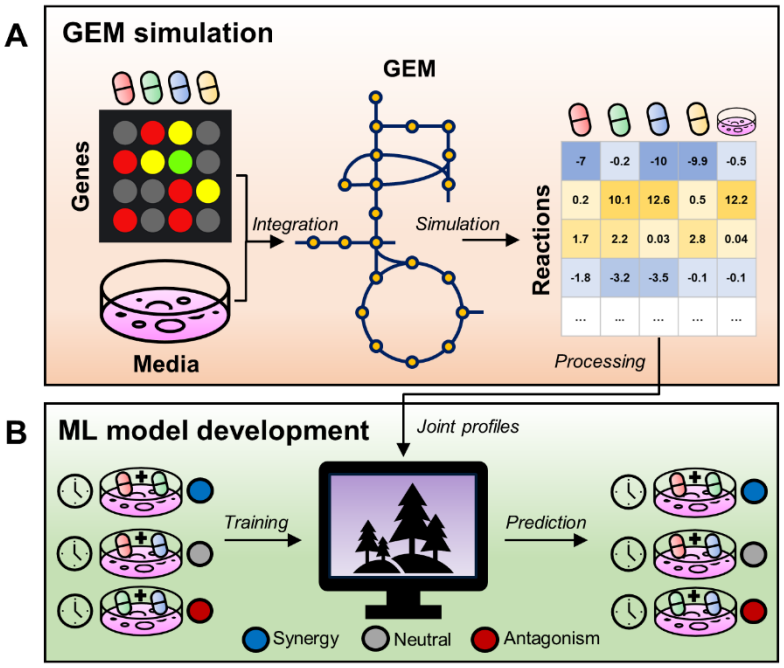

Fig. 1. CARAMeL approach schematic. The *Condition-specific Antibiotic Regimen Assessment using Mechanistic Learning* (CARAMeL) approach involves a two-step process: (**A**) omics data (e.g., transcriptomics) measured for single drug treatments and information on growth media composition are integrated into a genome-scale metabolic model (GEM) to simulate metabolic flux changes. (**B**) This information, along with drug interaction data, serve as inputs to train a machine learning (ML) model to predict outcomes for novel drug interactions.

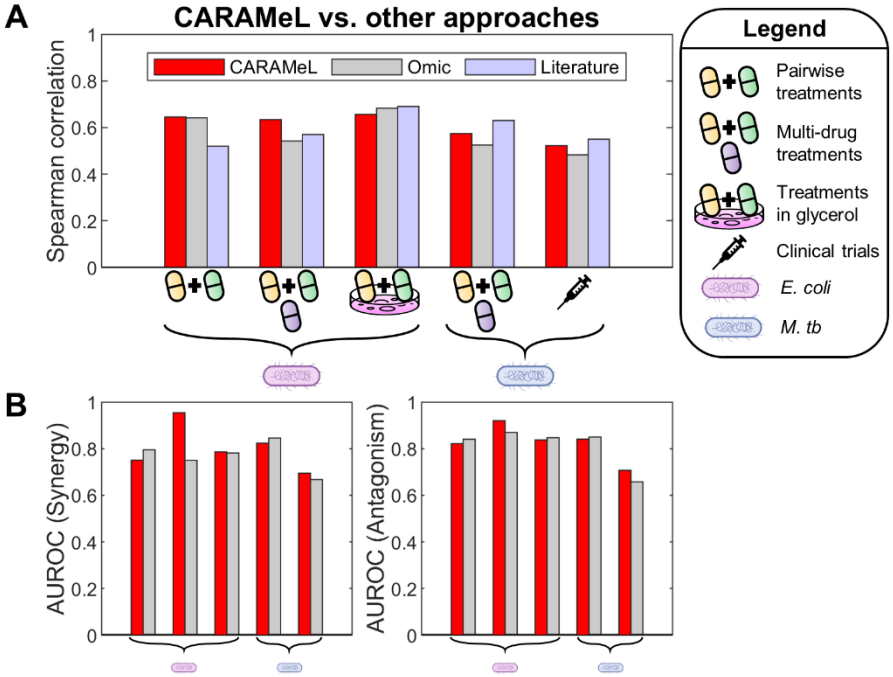

Fig. 2. CARAMeL was benchmarked against other predictive approaches. Model results for three approaches are reported: CARAMeL (this study), omics (based on chemogenomic or transcriptomic data as input), and literature (reported in literature). Model results were quantified based on (**A**) the Spearman correlation between actual outcomes and model predictions, and (**B**) the area under the receiver operating curve (AUROC) for classifying interactions as synergistic or antagonistic. Direct comparison to literature results is only shown for Spearman correlation.

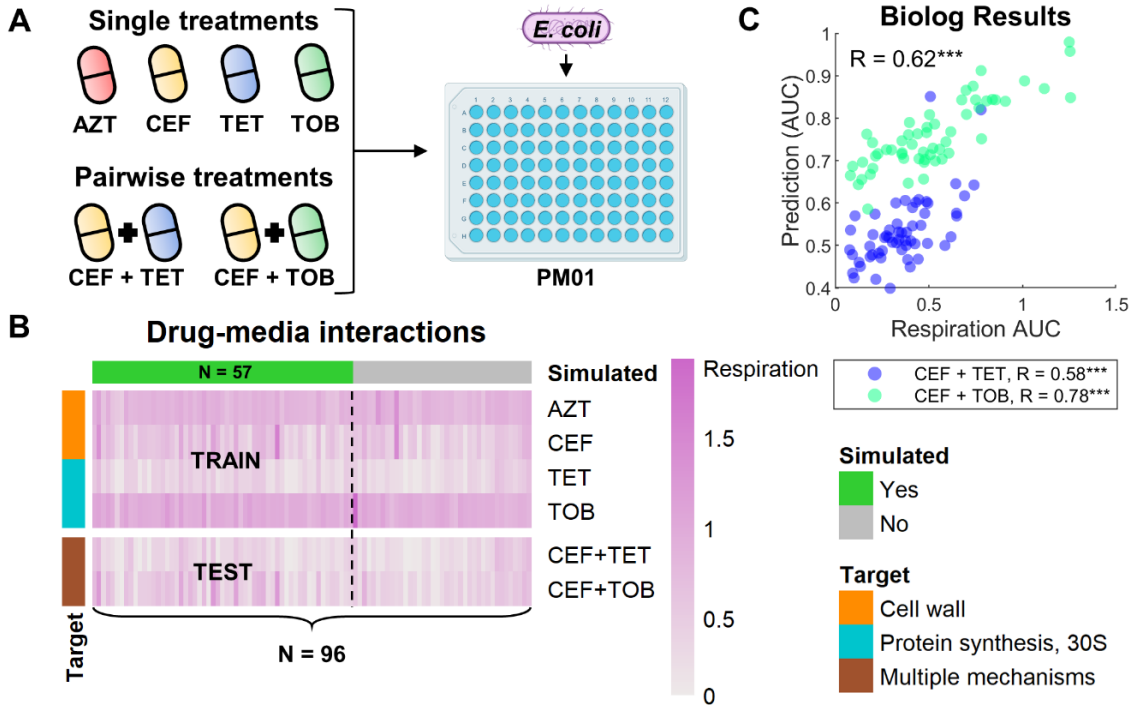

Fig. 3. CARAMeL accurately predicted drug interaction outcomes in 57 carbon sources. (**A**) *E. coli* was cultured in 96 carbon sources (Biolog PM01 plate), then treated with four single drug treatments (AZTreonam, CEFoxitin, TETtracycline, TOBramycin) and two pairwise treatments (CEF + TET and CEF + TOB). (**B**) Heatmap of metabolic activity (measured based on the respiration ratio between treatment vs. control) in response to all experimental perturbations. (**C**) Spearman correlation between experimental outcome and model predictions for all combinations in the test set are shown. *** p-value < 10^{-3}.

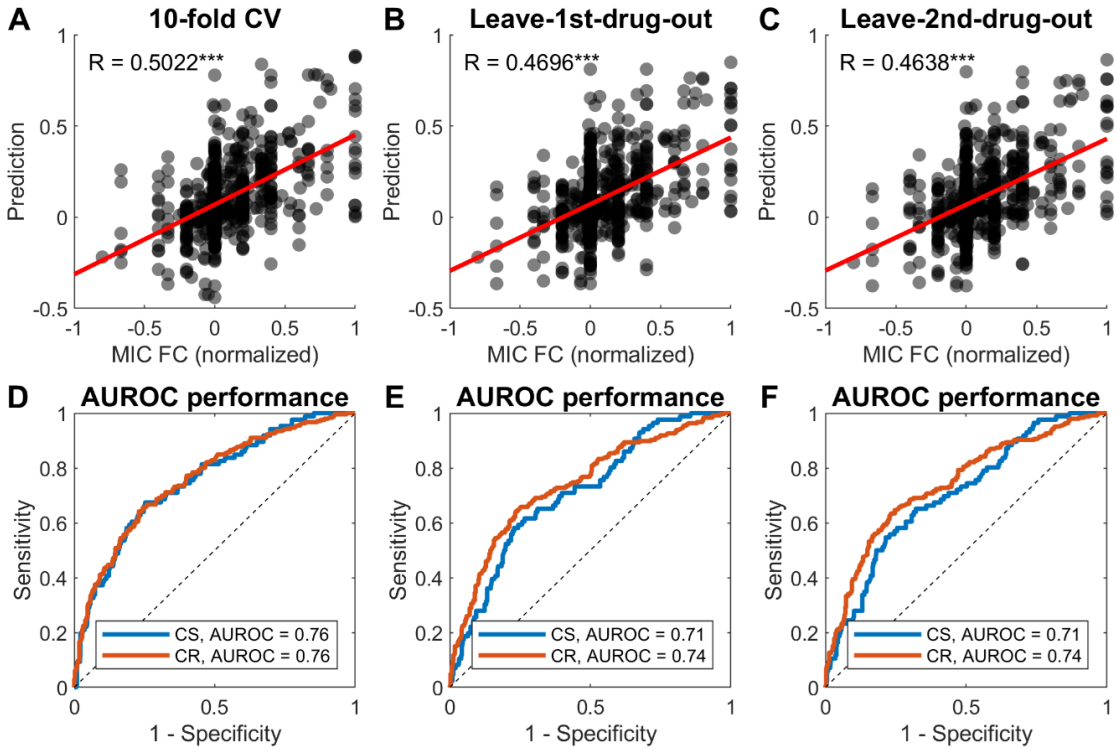

Fig. 4. 10-fold cross-validation and leave-out analysis results for sequential drug interactions. CARAMeL model performance for (**A, D**) 10-fold cross-validation, (**B, E**) leave-first-drug-out, and (**C, F**) leave-second-drug-out analyses. MIC: minimal inhibitory concentration; FC: fold-change, CS: collateral sensitivity, CR: cross-resistance. ***p-value < 10^{-3}.

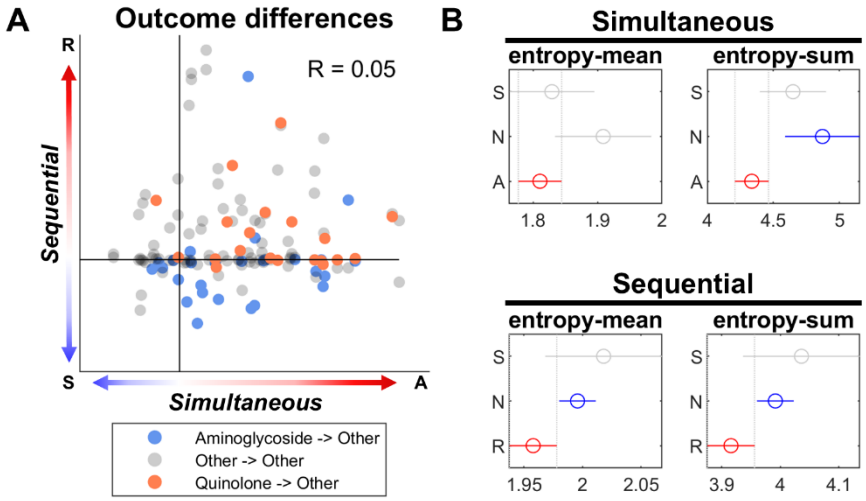

Fig. 5. Treatment time and metabolic entropy are highly predictive of combination therapy outcomes. (**A**) Interaction outcomes considerably differ between simultaneous and sequential treatments. (**B**) Drug combinations that lead to antagonism (A) or cross-resistance (R) result in less metabolic disarray compared to neutral (N) treatments and those leading to synergy or collateral sensitivity (S). Each line with a circle represents the 95% confidence interval of the entropy score for a particular group. Color difference indicates significant differences between intervals (ANOVA, $p < 0.05$).

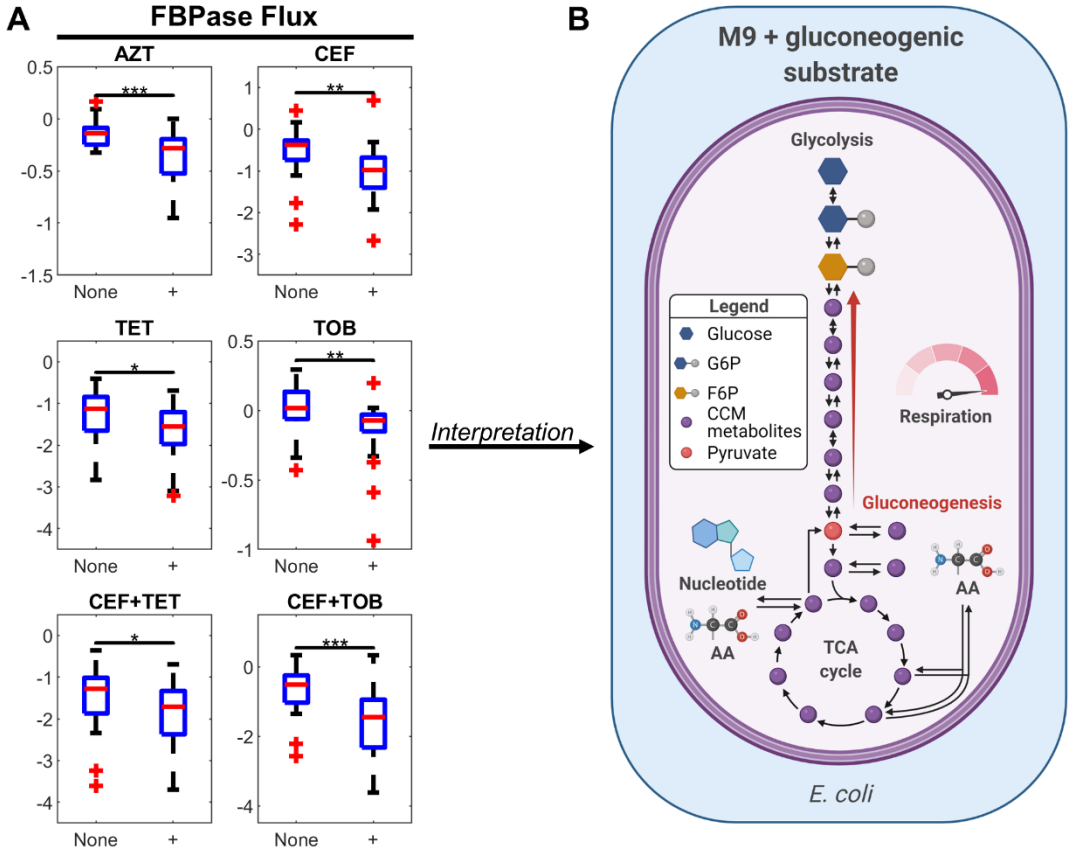

Fig. 6. The growth environment influences antibiotic treatment potency. (**A**) Positive flux through fructose 1,6-bisphosphatase (FBPase) was associated with increased potency for all six drug treatments assessed in the Biolog experiment. (**B**) Gluconeogenesis is activated during growth in minimal media (M9) supplemented with carbon sources downstream of pyruvate. This leads to increased respiration that enhances antibiotic efficacy compared to carbon sources that are directly converted to glucose, such as sugars. AZT: aztreonam, CEF: cefoxitin, TET: tetracycline, TOB: tobramycin, AUC: area under the curve, TCA: tricarboxylic acid, G6P: glucose 6-phosphate, F6P: fructose 6-phosphate, CCM: central carbon metabolism.

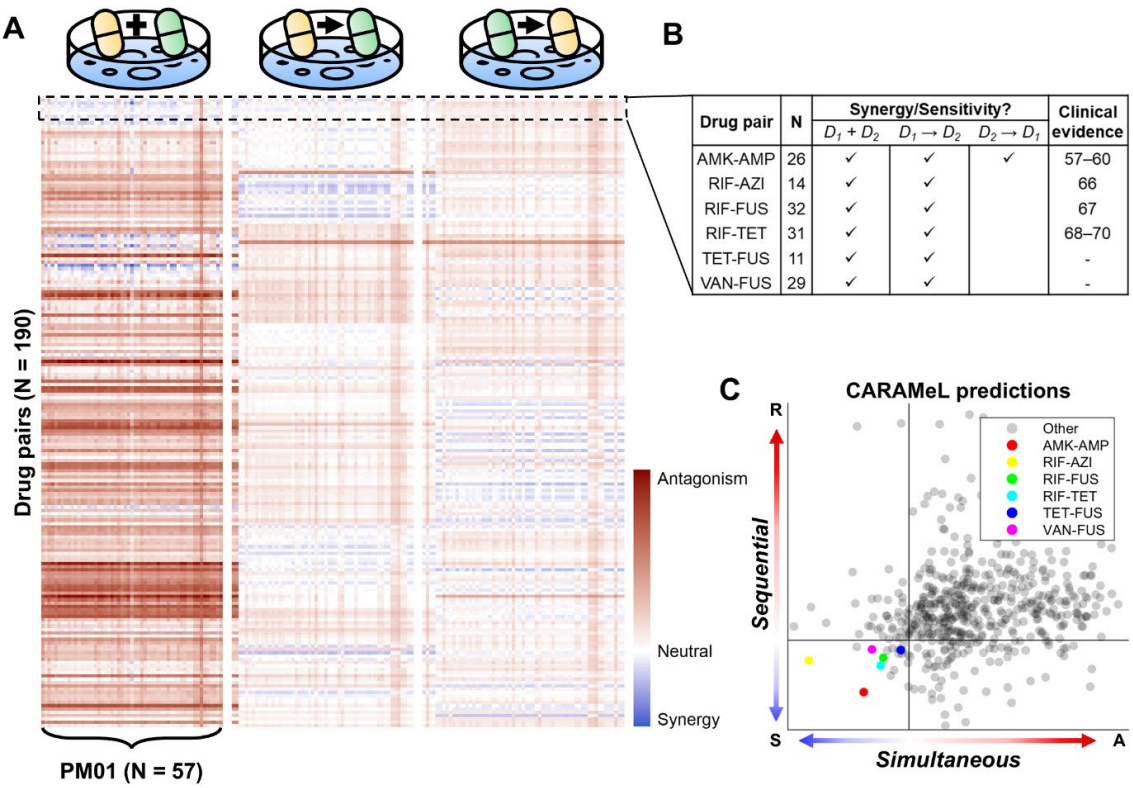

Fig. 7. CARAMeL prediction of pairwise combination therapy landscape. (**A**) Out of 528 drug pairs, 190 were predicted to yield synergy (IS < 0) for at least one case (i.e., cell). (**B**) Six of these were predicted to be robustly synergistic across time scales (simultaneous and sequential) and growth conditions (N > 10), with four possessing clinical evidence for efficacy. (**C**) Visual comparison of the lowest predicted interaction scores for simultaneous vs. sequential interactions for all drug pairs that were screened (N = 528). AMK: amikacin, AMP: ampicillin, AZI: azithromycin, FUS: fusidic acid, RIF: rifampicin, TET: tetracycline, VAN: vancomycin, N: number of growth conditions yielding synergy, S: synergy, A: antagonism, R: cross-resistance.

Table 1. Metabolic pathways enriched amongst top predictors for the *E. coli* CARAMeL model. Pathway enrichment was determined based on 652 features explaining 95% of the variance in model predictions. These features mapped to 360 reactions in the *E. coli* GEM iJO1366, out of which 244 had differential flux that significantly distinguished between synergy and antagonism (two-sample t-test, p-value < 0.05). Based on this 244-reaction list, 13 pathways were found to be significantly enriched (hypergeometric test, p-value < 0.05). N = number of reactions in pathway, Ratio = N / total reactions in pathway, P-value = hypergeometric test p-value.

Pathway	N	Ratio	P-value
Pyruvate Metabolism	7	0.70	2E-07
Nucleotide Salvage Pathway	29	0.21	8E-06
Inorganic Ion Transport and Metabolism	22	0.20	2E-04
Oxidative Phosphorylation	13	0.25	2E-04
Pentose Phosphate Pathway	5	0.42	4E-04
Transport, Outer Membrane	11	0.24	8E-04
Citric Acid Cycle	4	0.29	7E-03
Glycine and Serine Metabolism	4	0.29	7E-03
Alternate Carbon Metabolism	26	0.13	3E-02
Anaplerotic Reactions	2	0.25	3E-02
Folate Metabolism	2	0.22	5E-02
Glyoxylate Metabolism	1	0.25	5E-02
Glycolysis/Gluconeogenesis	4	0.18	5E-02

Supplementary Materials for

An interpretable flux-based machine learning model of drug interactions across metabolic space and time

Carolina H. Chung & Sriram Chandrasekaran*

*Corresponding author. Email: csriram@umich.edu

This PDF file includes:

Figs. S1 to S4
Tables S1 to S6
Data S1 to S5

Other Supplementary Materials for this manuscript include the following:

Data S1 to S5

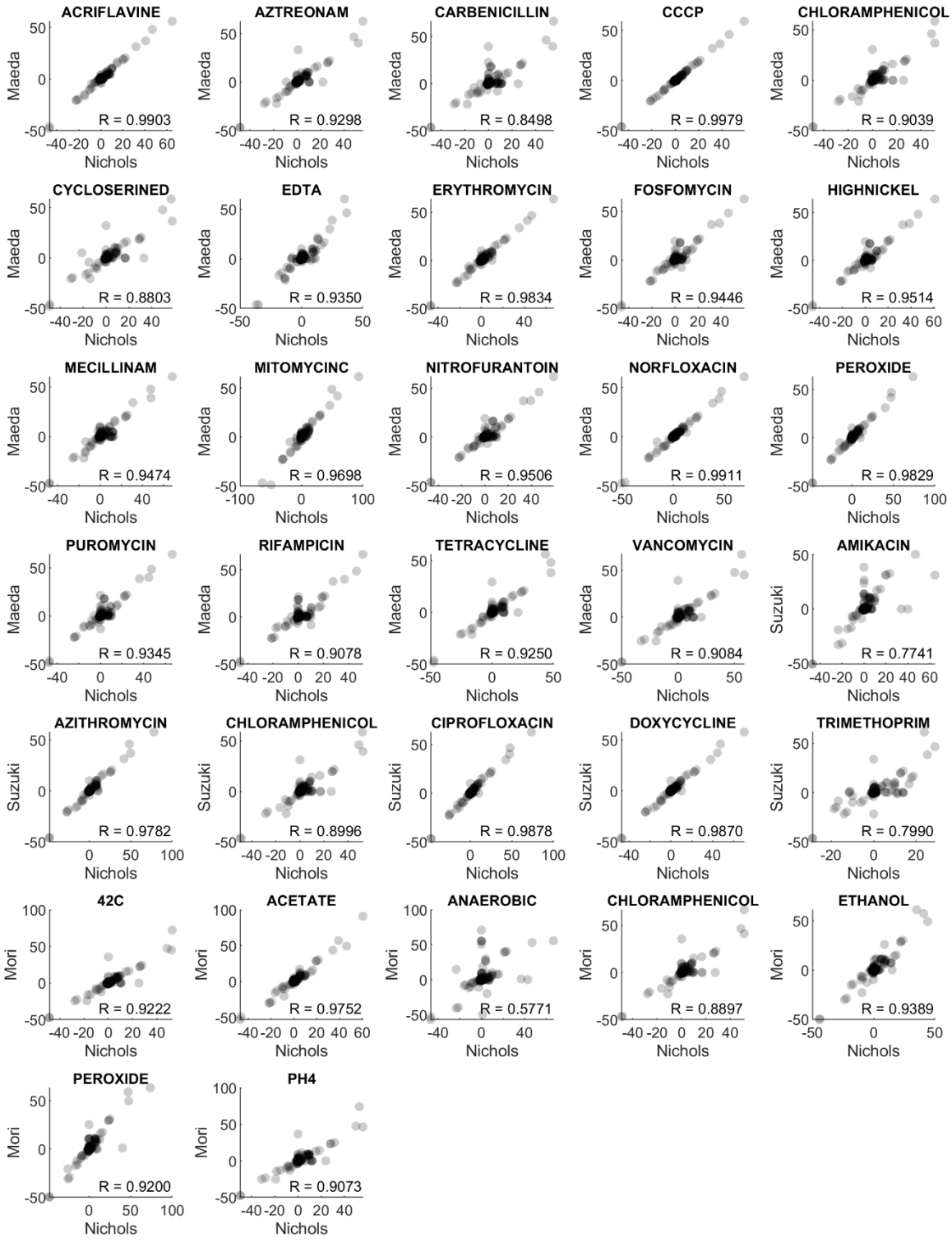

Fig. S1.

Flux profile comparison between different omic-based simulations. Correlations based on Pearson's method (all yielded $p << 10^{-3}$). All plots possess the same number of points (i.e., reactions, N = 2583). Nichols: chemogenomic-based (*35*), Maeda: transcriptomic-based (*37*), Suzuki: transcriptomic-based (*38*), Mori: proteomic-based (*39*).

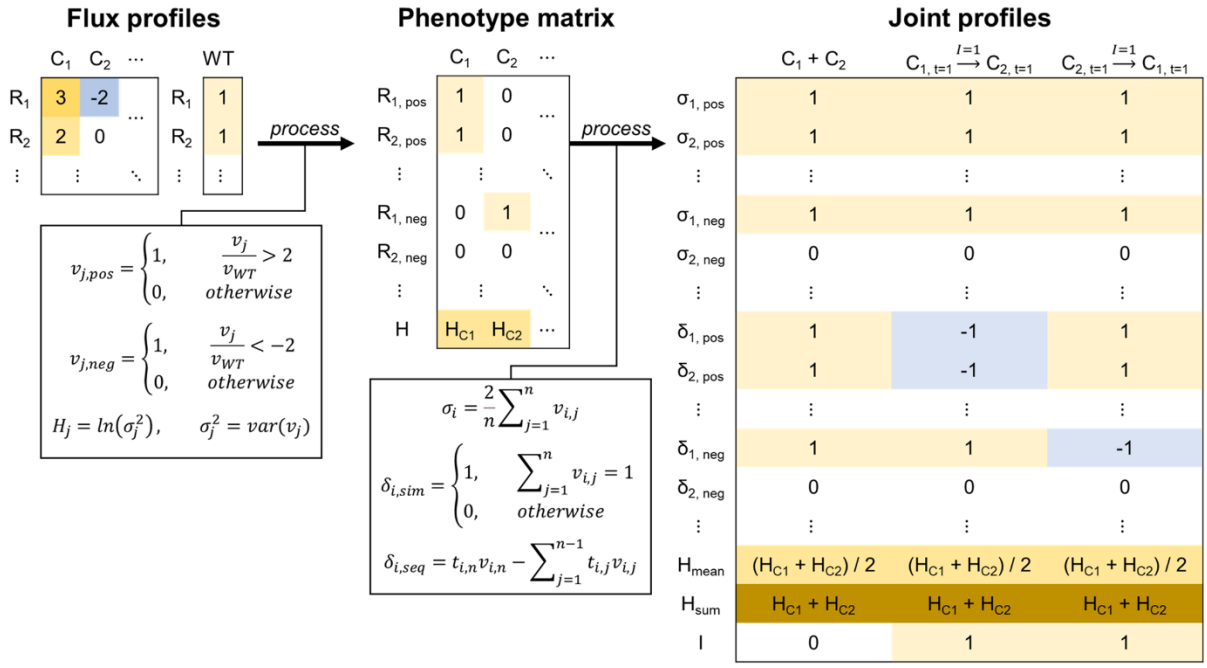

Fig. S2.

Schematic of flux data processing into joint profiles. Flux data (v) simulated from genome-scale metabolic models is binarized according to differential flux (either positive or negative) in comparison to wild type (WT, i.e., reference). These binarized flux profiles, along with the entropy (H) calculated for each condition (C), define the phenotype matrix which is subsequently processed into joint profiles. The sigma (σ) definition is the same between simultaneous (sim) and sequential (seq) interactions, while the delta (δ) definition differs depending on the interaction type. R = reaction, I = time interval, n = number of conditions in a combination.

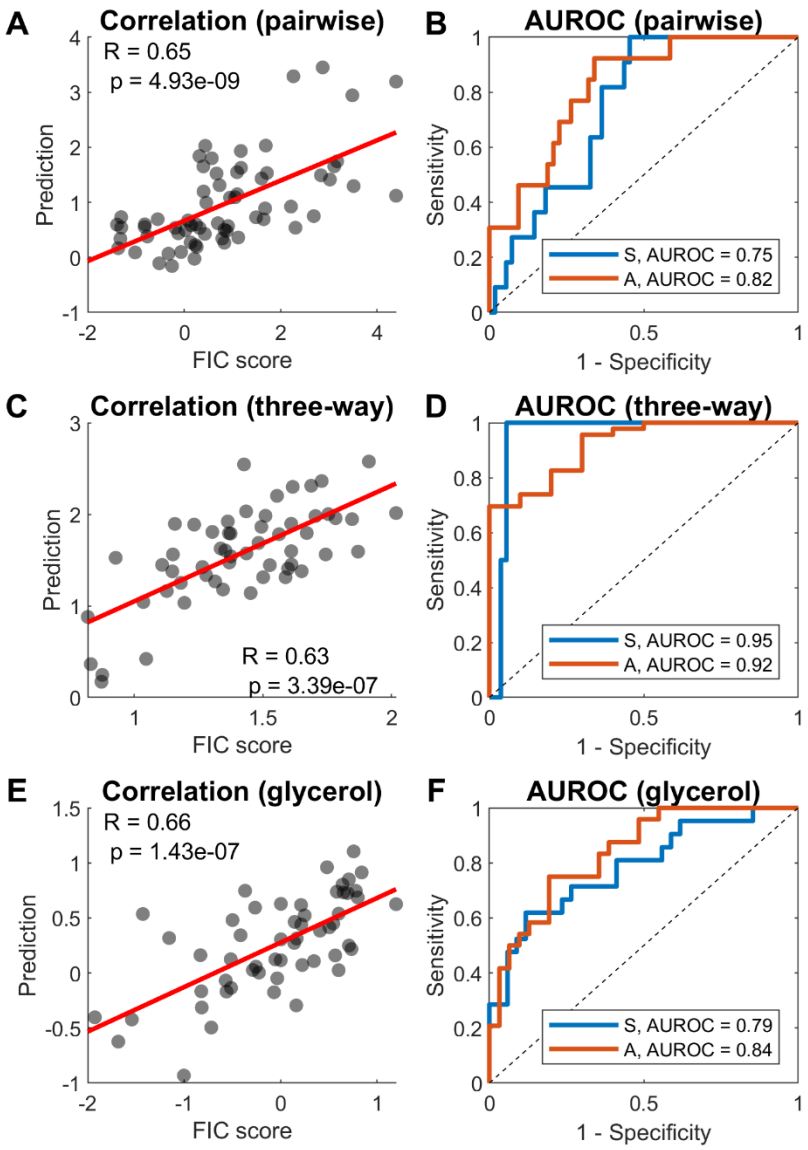

Fig. S3.

CARAMeL results for *E. coli* drug interaction data. Model performance results visualized as scatter and receiver operating curve (ROC) plots are shown for predicting (**A-B**) pairwise interactions, (**C-D**) three-way interactions, and (**E-F**) pairwise interactions in M9 glycerol. AUROC: area under the receiver operating curve. FIC: fractional inhibitory concentration, S: synergy, A: antagonism.

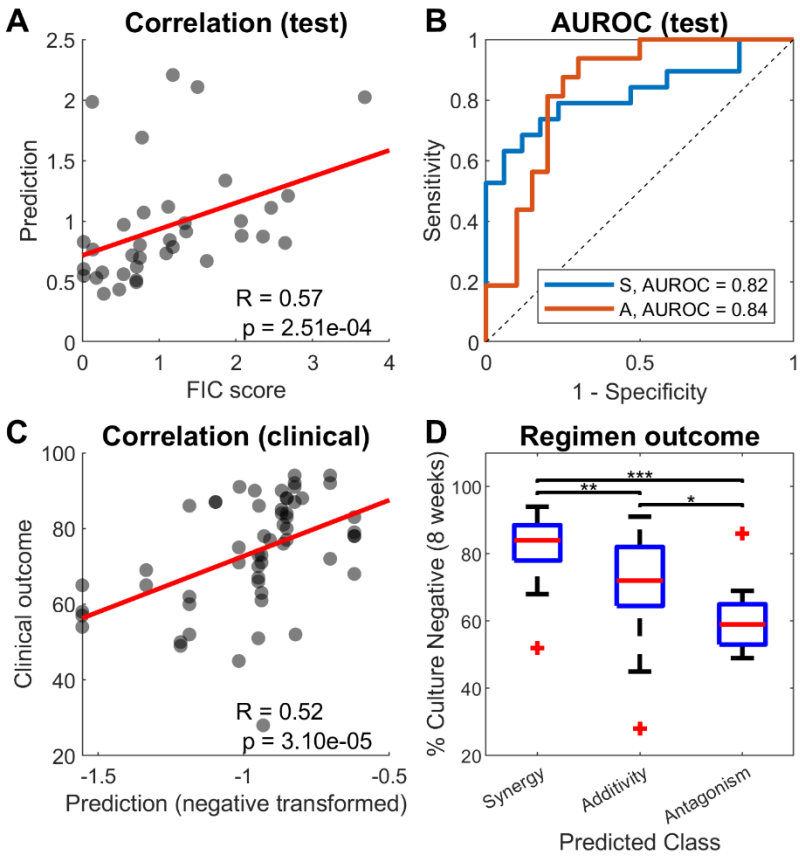

Fig. S4.

CARAMeL results for M. tb drug interaction data. (**A-B**) Model performance results visualized as scatter and receiver operating curve (ROC) plots are shown for predicting multi-drug interactions measured experimentally. (**C**) Inverted model predictions for 57 TB regimens prescribed in clinical trials correlate with clinical efficacy. (**D**) Predictions classified as synergistic capture most of the efficacious treatments (sputum clearance > 80%). AUROC: area under the receiver operating curve, ** p-value < 0.01, *** p-value < 0.001 (unpaired t-test). FIC: fractional inhibitory concentration, AUROC: area under the receiver operating curve, S: synergy, A: antagonism.

Table S1.

List of antibiotics used in *E. coli* drug interaction datasets. Abb.: abbreviation.

				Dataset					
Compound	**Abb.**	**Target**	**Class**	**Pair (train)**	**Pair (test)**	**Three-way**	**LB**	**Glucose**	**Glycerol**
Amikacin	AMK	Protein synthesis, 30S	Aminoglycoside	✓	✓				✓
Gentamicin	GEN			✓	✓				
Spectinomycin	SPE				✓		✓	✓	✓
Tobramycin	TOB			✓	✓				
Minocycline	MIN		Tetracycline			✓			
Tetracycline	TET			✓	✓		✓	✓	✓
Azithromycin	AZI	Protein synthesis, 50S	Macrolide			✓	✓	✓	✓
Chlarythromycin	CLA			✓	✓				
Erythromycin	ERY			✓	✓				
Chloramphenicol	CHL		Phenylpropanoid	✓	✓	✓	✓	✓	✓
Ciprofloxacin	CIP	DNA gyrase	Quinolone	✓	✓	✓			
Levofloxacin	LEV			✓	✓				
Nalidixic acid	NAL			✓	✓	✓			✓
Ampicillin	AMP	Cell wall	Beta-lactam			✓	✓	✓	✓
Aztreonam	AZT						✓	✓	✓
Cefoxitin	CEF			✓	✓				✓
Oxacillin	OXA			✓	✓				
Vancomycin	VAN		Glycopeptide		✓				
Fusidic acid	FUS	Elongation factor	Fusidane		✓				
Trimethoprim	TMP	Folic acid biosynthesis	Pyrimidine	✓	✓				
Rifampicin	RIF	RNA synthesis	Rifampin		✓	✓	✓	✓	✓
Nitrofurantoin	NIT	Multiple mechanisms	Furan	✓	✓	✓			
Triclosan	TRI		Phenol				✓	✓	✓
Hydrogen peroxide	H22	Oxidative stress	Stress	✓	✓				

Table S2.

List of antibiotics used in *M. tb* drug interaction datasets. Abb.: abbreviation, PTM: post-translational modification. * Putative mechanism.

				Dataset		
Compound	**Abb.**	**Target**	**Class**	**Train**	**Test**	**Clinical**
Sutezolid	SUTx	Protein synthesis, 23S	Oxazolidinone	✓		
Amikacin	AMK	Protein synthesis, 30S	Aminoglycoside	✓		
Kanamycin	KAN			✓		
Spectinomycin	SPE			✓	✓	
Streptomycin	SM			✓	✓	✓
Minocycline	MIN		Tetracycline	✓		
Tetracycline	TET			✓		
Azithromycin	AZI	Protein synthesis, 50S	Macrolide	✓		
Chlarythromycin	CLA			✓	✓	
Erythromycin	ERY			✓		
Roxithromycin	ROX			✓		
Linezolid	LZDx		Oxazolidinone	✓		
Chloramphenicol	CHL		Phenylpropanoid	✓		
Ciprofloxacin	CIP	DNA gyrase	Quinolone	✓	✓	
Levofloxacin	LEV			✓	✓	
Moxifloxacin	MOX			✓	✓	✓
Norfloxacin	NFX				✓	
Ofloxacin	OFX1			✓		✓
Novobiocin	NOV		Glycoside	✓		
Ampicillin	AMP	Cell wall	Beta-lactam	✓		
Oxacillin	OXA			✓		
Vancomycin	VAN		Glycopeptide	✓		
Cefaclor	CFL		Cephalosporin	✓		
SQ109	SQ109		Ethylenediamine	✓		
Isoniazid*	INH		Hydrazine	✓	✓	✓
Econazole	ECO		Imidazole	✓		
Pretomanid	PA824			✓		✓
Ethionamide*	ETH		Isonicotinic acid	✓		
Cycloserine D	CSD		Serine	✓		
PBTZ169	PBTZ169x		Thiazine	✓		
Capreomycin	CAP	Multiple mechanisms	Peptide	✓	✓	
Clofazimine*	CFZ		Phenazine	✓	✓	
Fusidic acid	FUS	Elongation factor	Fusidane	✓		
Ethambutol	EMBx	RNA synthesis	Ethylenediamine	✓		✓
Rifampicin	RIF		Rifampin	✓	✓	✓
Rifapentine	RIFP		Rifamycin			✓
Bedaquiline	BDQ	ATP synthase	Diarylquinoline	✓	✓	

Ethium bromide	EB	DNA structure	Phenanthridine	✓		
Pyrazinamide*	PZA	Fatty acid synthase	Pyrazine			✓
Menadione	MEN	PTM	Vitamin	✓		
Verapamil	VERx	Calcium channels	Phenethylamine	✓		
Thioridazine	THZ	Synaptic activity	Phenothiazine	✓		
Chlorpromazine	CPZ			✓	✓	

Table S3.

Drug information for Biolog experiment. Abb.: abbreviation, Conc.: drug concentration.

					Conc. (μg/mL)	
Compound	**Abb.**	**Target**	**Class**	**Type**	*Single*	*Pairwise*
Aztreonam	AZT	Cell wall	Beta-lactam	Bactericidal	0.03	-
Cefoxitin	CEF			Bactericidal	1.87	1.87
Tetracycline	TET	Protein synthesis, 30S	Tetracycline	Bacteriostatic	1.42	1.42
Tobramycin	TOB		Aminoglycoside	Bactericidal	0.15	0.15

Table S4.

List of antibiotics used in sequential drug interaction datasets for *E. coli*. Abb.: abbreviation.

				Time scale		
Compound	**Abb.**	**Target**	**Class**	*T = 10*	*T = 21*	*T = 90*
Amikacin	AMK	Protein synthesis, 30S	Aminoglycoside	✓	✓	✓
Gentamicin	GEN			✓		✓
Spectinomycin	SPE				✓	
Streptomycin	SM			✓	✓	✓
Tobramycin	TOB				✓	
Doxycycline	DOX		Tetracycline		✓	✓
Minocycline	MIN			✓		✓
Tetracycline	TET			✓	✓	✓
Azithromycin	AZI	Protein synthesis, 50S	Macrolide	✓		✓
Erythromycin	ERY				✓	
Spiramycin	SPI				✓	
Chloramphenicol	CHL		Phenylpropanoid	✓	✓	✓
Ciprofloxacin	CIP	DNA gyrase	Quinolone	✓	✓	✓
Levofloxacin	LEV			✓		✓
Nalidixic acid	NAL			✓	✓	✓
Norfloxacin	NOR					✓
Ampicillin	AMP	Cell wall	Beta-lactam	✓	✓	
Cefoxitin	CEF				✓	
Ceftazidime	CFZ					✓
Amoxicillin	AMX			✓		
Sulfamonomethoxine	SMM	Folic acid biosynthesis	Sulfonamide		✓	
Trimethoprim	TMP		Pyrimidine	✓	✓	✓
Nitrofurantoin	NIT	Multiple mechanisms	Furan	✓	✓	
Fosfomycin	FOS	Cell wall biogenesis	Phosphonic acid	✓		
Fusidic acid	FUS	Elongation factor	Fusidane		✓	
Polymyxin B	PMB	Lipopolysaccharide	Peptide	✓		
Rifampicin	RIF	RNA synthesis	Rifampin	✓		✓

Table S5.

Constraint-based modeling (CBM) parameter optimization results. * Chosen parameters for *M. tb*, + chosen parameters for *E. coli*. CV-R: 10-fold cross-validation correlation in the training dataset, GR-V: variance in growth rate, NG-P: percentage of no growth (GR = 0) conditions.

	CBM parameters			***E. coli* results**			***M. tb* results**		
	Kappa	*Rho*	*Epsilon*	*CV-R*	*GR-V*	*NG-P*	*CV-R*	*GR-V*	*NG-P*
	0.001	0.001	0.001	0.4055	0	0	0.3640	0	0
	0.01	0.01	0.001	0.3260	0.0074	0	0.5024	0.0003	0.0233
	0.1	0.1	0.001	0.4077	0.0634	0	0.4858	0.0005	0.0698
	1	1	0.001	0.4313	0.2022	0.3636	0.4409	0.0005	0.0698
	0.001	0.001	0.01	0.4260	0	0	0.4124	0	0
*	**0.01**	**0.01**	**0.01**	0.3739	0.0091	0	0.5207	0.0003	0.1395
	0.1	0.1	0.01	0.389	0.0670	0	0.5149	0.0004	0.6977
	1	1	0.01	0.4189	0.1866	0.4848	0.5242	0.0003	0.7674
	0.001	0.001	0.1	0.6406	0	0	0.5231	0	0
	0.01	0.01	0.1	0.4090	0.0095	0	0.4959	0.0001	0.5581
	0.1	0.1	0.1	0.3978	0.1056	0.0606	0.4792	0.0001	0.7907
	1	1	0.1	0.3869	0.1294	0.5152	0.4471	0.0001	0.8837
	0.001	0.001	1	0.3860	0	0	0.4620	0	0
+	**0.01**	**0.01**	**1**	0.6512	0.0113	0	0.5131	0.0003	0.6047
	0.1	0.1	1	0.6150	0.0994	0.0909	0.5270	0	0.8140
	1	1	1	0.6294	0.0765	0.5758	0.5099	0	0.9070

Table S6.

Benchmarking correlation results based on different constraint-based modeling (CBM) parameter choices. * Chosen parameters for *M. tb*, + chosen parameters for *E. coli*. R1: pairwise interactions (*27*), R2: three-way interactions (*28*), R3: glycerol interactions (*28*), R4: pairwise and three-way interactions (*29*), R5: pairwise to five-way TB clinical regimens (*40*).

	CBM parameters			*E. coli* results			*M. tb results*	
	Kappa	*Rho*	*Epsilon*	*R1*	*R2*	*R3*	*R4*	*R5*
	0.001	0.001	0.001	0.2884	0.4441	0.5781	0.6370	0.5535
	0.01	0.01	0.001	0.5032	0.3516	0.5092	0.5873	0.4369
	0.1	0.1	0.001	0.4676	0.3666	0.5715	0.4946	0.2304
	1	1	0.001	0.5115	0.4001	0.5421	0.4717	0.4135
	0.001	0.001	0.01	0.3726	0.3636	0.5544	0.4638	0.5361
*	**0.01**	**0.01**	**0.01**	0.4525	0.2447	0.5900	0.5256	0.5445
	0.1	0.1	0.01	0.5390	0.2599	0.5514	0.4858	0.2642
	1	1	0.01	0.3899	0.3460	0.5915	0.4730	0.4124
	0.001	0.001	0.1	0.5421	0.5809	0.5669	0.5382	0.4483
	0.01	0.01	0.1	0.5829	0.5023	0.6281	0.6335	0.4263
	0.1	0.1	0.1	0.3313	0.3762	0.6382	0.5942	0.5140
	1	1	0.1	0.1545	0.4375	0.6745	0.5560	0.4982
	0.001	0.001	1	0.1772	0.1372	0.2668	0.3253	0.5380
+	**0.01**	**0.01**	**1**	0.6445	0.6216	0.6641	0.4884	0.4870
	0.1	0.1	1	0.6057	0.6536	0.6650	0.4947	0.4788
	1	1	1	0.6352	0.6169	0.6101	0.4939	0.3726

Data S1. (separate file)

Top CARAMeL features explaining 95% of the variance in model predictions.

Data S2. (separate file)

iJO1366 reactions explaining 95% of the variance between actual and predicted interaction outcomes.

Data S3. (separate file)

Carbon sources in Biolog PM01 plate for which flux data was simulated.

Data S4. (separate file)

CARAMeL predictions for 30,096 drug-drug-media interactions in three time scales (N = 90,288).

Data S5. (separate file)

Drug combinations predicted to yield synergy or collateral sensitivity in at least one metabolic condition. N = number of conditions where both synergy and collateral sensitivity were predicted.